



Satellite-derived bathymetry using the ICESat-2 lidar and Sentinel-2 imagery datasets

Yue Ma^{a,b,c}, Nan Xu^d, Zhen Liu^{e,*}, Bisheng Yang^{f,*}, Fanlin Yang^a, Xiao Hua Wang^{c,g}, Song Li^b

^a College of Geodesy and Geomatics, Shandong University of Science and Technology, Qingdao 266590, China

^b School of Electronic Information, Wuhan University, Wuhan 430072, China

^c School of Science, University of New South Wales, Canberra BC 2610, Australia

^d College of Marine Science and Engineering, Nanjing Normal University, Nanjing 210023, China

^e College of Ocean Science and Engineering, Shandong University of Science and Technology, Qingdao 266590, China

^f State Key Laboratory of Information Engineering in Surveying, Mapping and Remote Sensing, Wuhan University, Wuhan 430072, China

^g Sino Australian Research Consortium for Coastal Management, the University of New South Wales, Canberra BC 2610, Australia

ARTICLE INFO

Keywords:

Bathymetry
Photon-counting lidar
Sentinel-2
ICESat-2
Empirical model
South China Sea

ABSTRACT

Accurate bathymetric data is essential for marine, coastal ecosystems, and related studies. In the past decades, a lot of studies were investigated to obtain bathymetric data in shallow waters using satellite remotely sensed data. Satellite multispectral imagery has been widely used to estimate shallow water depths based on empirical models and physics-based models. However, the *in-situ* water depth information is essential (as the *priori*) to use the empirical model in a specific area, which limits its application, especially for remote reefs. In this study, the bathymetric maps in shallow waters were produced based on empirical models with only satellite remotely sensed data (i.e., the new ICESat-2 bathymetric points and Sentinel-2 multispectral imagery). The bathymetric points from the spaceborne ICESat-2 lidar were used in place of the *in-situ* auxiliary bathymetric points to train the classical empirical models (i.e., the linear model and the band ratio model). The bathymetric points were firstly extracted from noisy ICESat-2 raw data photons by an improved point cloud processing algorithm, and then were corrected for bathymetric errors (which were caused by the refraction effect in the water column, the refraction effect on the water surface, and the fluctuation effect on the water surface). With the trained empirical models and Sentinel-2 multispectral images, the bathymetric maps were produced for Yongle Atoll, in the South China Sea and the lagoon near Acklins Island and Long Cay, to the southeast of Bahama with four-date Sentinel-2 images. The bathymetry performance (including the accuracy and consistency of multi-date data) was evaluated and compared with the *in-situ* measurements. The results indicate that the bathymetric accuracy is well, and the RMSE is lower or close to 10% of the maximum depth for the two models with four-date images in two study areas. The consistency of multi-date data is well with the mean R^2 of 0.97. The main novelties of this study are that the accuracy bathymetric points can be obtained from the ICESat-2 raw data using the proposed signal processing and error correction method, and using the ICESat-2 bathymetric points, the satellite multispectral imagery based on empirical models is no longer limited by local *priori* measurements, which were essential in previous studies. Hence, In the future, with the help of free and open-access satellite data (i.e., ICESat-2 data and Sentinel-2 imagery), this approach can be extended to a larger scale to obtain bathymetric maps in the shallow water of coastal areas, surroundings of islands and reefs, and inland waters.

1. Introduction

As the interaction zone between sea and land or surroundings of islands and reefs, shallow water provides a fundamental physical environment for marine and coastal ecosystems for their sustainability and biodiversity, especially under the global warming and sea level rise (Kutser et al., 2003; Hoegh-Guldberg et al., 2007; Nicholls and

Cazenave, 2010). The underwater topography is an effective indicator to characterize shallow waters of the marine and coastal environment (Kulp and Strauss, 2019; Dong et al., 2019). High-resolution bathymetric data is a fundamental reference for a wide range of coastal applications, e.g., the near-shore geomorphology, sediment process, fishing, hydrology, mineral exploration, cable routing, coastal planning, and hydrodynamic model developing. Meanwhile, since ancient times,

* Corresponding authors.

E-mail addresses: zhliu01@126.com (Z. Liu), bshyang@whu.edu.cn (B. Yang).

coastal areas provide space for large and growing concentrations of human population, settlements and economic activities. Traditionally, shallow water topographic surveys primarily relied on the single-beam or multiple-beam echo sounder based on a ship-based platform (Yang et al., 2017a; Shang et al., 2019). Airborne bathymetric lidars can quickly and accurately obtain the over and underwater topography in coastal areas (Irish and Lillycrop, 1999; Westfeld et al., 2017; Yang et al., 2017b). However, these approaches have some limitations in very remote or sensitive areas, where ships and aircrafts have difficulties be close to or reach.

With the development of spaceborne remote sensing technology, many remotely sensed data (e.g., the hyperspectral/multispectral imagery and the synthetic aperture radar (SAR)) have been applied to obtain the shallow water depth. Although SAR data might exhibit the advantage of covering a wider range of shallow water and can provide indirect depth information in some regions, specific requirements on spatial resolution, morphology and texture of seabed topography, slicks, waves, fronts, sea surface wind, and weather condition might limit its applications (Kutser et al., 2020; Mishra et al., 2014; Renga et al., 2014; Pereira et al., 2019). Only visible light is able to penetrate through the water column to capture information on water depth and benthic habitats (Kutser et al., 2020).

Satellite-derived bathymetry (SDB) is becoming a cost-effective way to rapidly and efficiently obtain large-scale and high-resolution bathymetry information (Cerdeira-Estrada et al., 2012; Cahalane et al., 2019). Some spaceborne hyperspectral sensors have been adopted to map the shallow water habitat and bathymetry. For example, the Hyperion and Hyperspectral Imager for the Coastal Ocean (HICO) images have been applied for mapping the water depth and bottom type simultaneously (Kutser et al., 2002; Kutser et al., 2006a, 2006b, 2006c; Lee et al., 2007; Garcia et al., 2014a, 2014b). Spaceborne multispectral sensors with different spatial-temporal resolutions (e.g., the Landsat-8, WorldView-2, Sentinel-2, GeoEye-1, Pleiades, IKONOS, Gaofen-2, etc.) have been used in bathymetry mapping around the world (Hedley et al., 2018; Jagalingam and Hedge, 2017; Casal et al., 2019; Poursanidis et al., 2019; Pike et al., 2019; Su et al., 2015; Liu et al., 2018; Chen et al., 2019; Raucoules et al., 2019; Traganos et al., 2018; Kerr and Purkis, 2018; Hamylton et al., 2015; Hochberg et al., 2003; Eugenio et al., 2015).

During the past decades, the SDB studies have developed from basic linear function to band ratios of logarithmic-transformed models, nonlinear inversion models and physics-based models (Lyzenga, 1981; Stumpf et al., 2003; Dekker et al., 2011; Cahalane et al., 2019). Different physics-based models have achieved good results in bathymetry and benthic mapping (Kutser et al., 2002; Kutser et al., 2006a, 2006b, 2006c; Mobley et al., 2005; Lesser and Mobley, 2007; Lee et al., 1998, 1999; Petit et al., 2017; Brando et al., 2009; Katja et al., 2016; Dörnhöfer et al., 2016a, 2016b; Gao, 2009; Giardino et al., 2014; Ohlendorf et al., 2011; Cerdeira-Estrada et al., 2012; Eugenio et al., 2015; Adler-Golden et al., 2005). Empirical models have been widely used in bathymetry mapping (Gholamalifard et al., 2013; Traganos et al., 2018; Yunus et al., 2019; Lyzenga, 1978; Paredes and Spero, 1983; Philpot, 1989; Lyzenga et al., 2006; Stumpf et al., 2003; Su et al., 2014; Manessa et al., 2018). However, the regional differences, sensor variations, and especially large requirements for *in-situ* data on water depths influence the performance of empirical models (Kutser et al., 2020).

The ICESat-2 (Ice, Cloud, and Land Elevation Satellite-2) carries the first spaceborne photon-counting lidar, i.e., the ATLAS (Advanced Topographic Laser Altimeter System), and was launched in September 2018. Benefiting from the much more sensitive photon-counting detectors and the green lasers that can penetrate water column, the ATLAS has achieved seafloor detections in depths of up to ~40 m in very clean waters (Parrish et al., 2019). The ICESat-2 ATLAS has three strong laser beams along-track (i.e., the left, central, and right beam) and the cross-track distance between adjacent beams is 3.3 km. With an

approximately 500 km altitude and 10 kHz laser repetition frequency, in the along-track direction, the interval between adjacent laser pulse on Earth's surface is approximately 0.7 m (Markus et al., 2017). After calibrating the bathymetric error and other errors, the spaceborne photon-counting lidars have a potential to achieve the sub-meter bathymetric accuracy in shallow and clean water areas (Parrish et al., 2019). Therefore, the ICESat-2 can provide plenty of accurate along-track bathymetric points wherever it flies over, and these bathymetric points are invaluable to serve as the *priori* water depth measurements to obtain bathymetric topography along with SDB empirical models.

However, in the standard ICESat-2 Level-2 datasets, although many kinds of errors have been corrected (e.g., the solid tide and the atmospheric delay), the bathymetric errors were not corrected, e.g., the sea level variabilities induced by waves and tides, the refraction effect of sloping sea surface and water column, the non-nadir incidence, and the scattering effect related to atmospheric conditions and inherent water properties (Jasinski et al., 2016; Li et al., 2019). For bathymetric errors of satellite photon-counting lidars, Parrish et al. (2019) has creatively investigated the horizontal and vertical errors of the refraction effect arising from the water column and the non-nadir incidence. The velocity of light in water column is less than that in atmosphere because of the difference of the refractive index. The incidence angles for the central beam and outer beams of the ICESat-2 is nearly 0° and only 0.38°, which means, the horizontal error of the refraction effect arising from the non-nadir incidence is 0.003D (where D is the water depth) and vertical error is negligible (Parrish et al., 2019). However, the effect of the water surface fluctuation and the refraction effect arising from the sea surface slope were not considered. The water surface is very fluctuating (i.e., the water level is changeable) and has a wave height (that can be up to meters) and a surface slope (that can be up to twenty degrees) at each point. The wave height and slope distribution are mainly influenced by the wind speed above the water surface (Tsai and Gardner, 1982). In addition, because of the sensitivity of ICESat-2 detectors, the raw data photons are very noisy (mainly due to the solar background), especially in the daytime. Consequently, an effective method is essential to detect the bathymetric signal photons from the raw noisy photons.

In this paper, combining the new ICESat-2 lidar datasets and the Sentinel-2 multispectral imagery, the bathymetric maps in shallow waters were produced with only satellite remotely sensed data via empirical models. The bathymetric points from the spaceborne ICESat-2 lidar were used in place of the *in-situ* auxiliary bathymetric points to train the classical empirical models (i.e., the linear model and the band ratio model). First, a method of point clouds processing was implemented to detect the bathymetric signal points from the noisy raw ICESat-2 data photons. Second, a calibration method was proposed to correct the bathymetric errors arising from the refraction effect in water column and on the water surface and caused by the fluctuation effect on the water surface for ICESat-2 datasets. Third, the calibrated ICESat-2 bathymetric points were taken as the *priori* measurements, which were matched with the preprocessed Sentinel-2 multispectral imagery, and the bathymetric maps were generated with the classical linear band model and the band ratio model in two study areas (near Yongle Atoll, South China Sea and near Acklins Island and Long Cay, to the southeast of Bahama). Finally, the obtained bathymetry performance (including the accuracy and consistency of multi-date data) was evaluated and compared with the *in-situ* measurements.

2. Study areas and data

2.1. Study areas and airborne *in-situ* data

In this study, two study areas with multi-date ICESat-2 and Sentinel-2 data are involved. As shown in Fig. 1, the first study area is Yongle Atoll (Latitude: 16.25°–16.40° N, Longitude: 111.30°–111.50° E) that locates in the southwestern part of Xisha archipelago in the South China

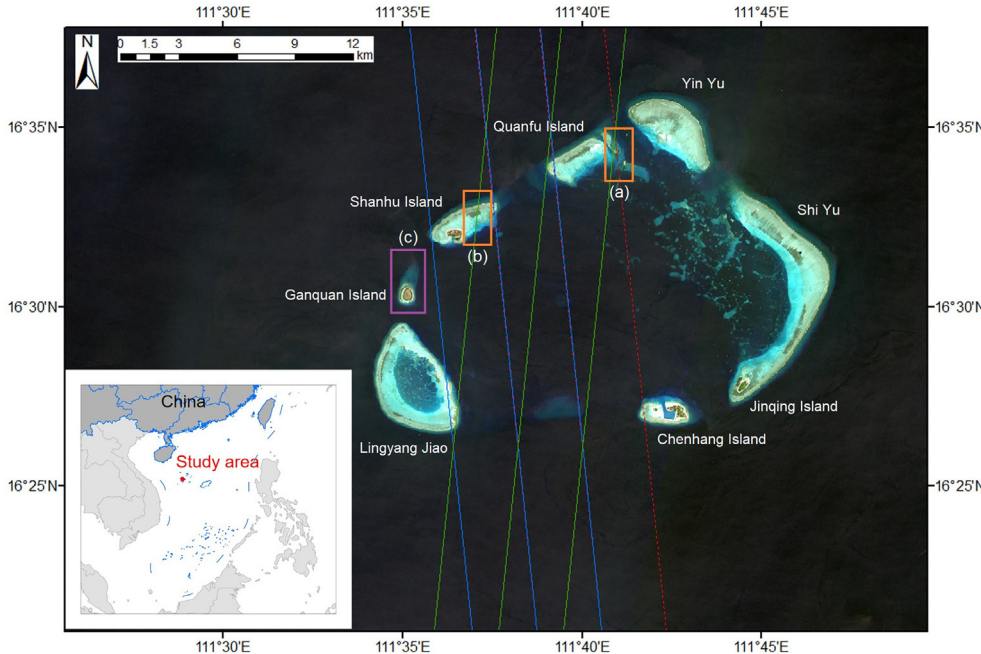


Fig. 1. ICESat-2 laser beam trajectories near Yongle Atoll, in the South China Sea. The satellite image used as a basemap is from the Sentinel-2 imagery on 24/02/2019. Three red trajectories, three green trajectories, and three blue trajectories correspond to the flight routes of ICESat-2 on 22/10/2018, 22/02/2019, and 12/04/2019, respectively. The two orange boxes (a) and (b) correspond to the two sampled areas (to illustrate the detailed ICESat-2 photons) in Fig. 5 (in daytime) and Fig. 6 (at night), respectively. The purple box marked by (c) near Ganquan Island illustrates the *in-situ* bathymetric measurements (that were used for validation) from an airborne bathymetric lidar. (For interpretation of the references to colour in this figure legend, the reader is referred to the web version of this article.)

Sea. Yongle Atoll is composed of several islands as well as some reefs and sandbanks, and the total area that is out of the water in Yongle Atoll is several km² (Xu et al., 2011). It has abundant aquatic resources and a convenient waterway in shallow lagoon inside the atoll.

In this area, the *in-situ* bathymetric data were captured by an airborne bathymetric lidar (the Optech Aquarius) in Ganquan Island, with the area of approximately 0.3 km² and in the purple box marked by (c) of Fig. 1 (Zhang et al., 2017). Ganquan Island is a typical coral island. Around Ganquan Island, the water depth is relatively shallow (within 20 m) and underwater topography has a gentle slope, but underwater topography is dramatically falling away from the island.

In late 2012, the Optech Aquarius lidar system worked at a flight altitude of 300 m around Ganquan Island (Su et al., 2019), i.e., only one-date *in-situ* measurement is available. Around the shallow water area of Ganquan Island, all bathymetric points were captured with a maximum depth of approximately 18 m. The size of laser footprints was approximately 0.3 m in diameter. The density of the captured laser points was approximately 4 points/m² and generally evenly distributed. The depth accuracy of this airborne *in-situ* measurement was approximately 35 cm (Yang et al., 2017b). It should be noted that the airborne *in-situ* measurements do not use to train the empirical models, but validate the accuracy of the satellite-derived bathymetric maps in Ganquan Island.

The second study area is the lagoon between the Acklins Island (the southeastern island in Fig. 2) and Long Cay (the northwestern island) and the surrounding waters outside these islands. The geographic location of this area has a range of Latitude: 22.10°–22.60° N and Longitude 73.90°–74.40° W. This study area locates to the southeast of Bahama. Inside and outside of the lagoon, the total shallow water area (within 25 m in depth) is approximately 1500 km² and mainly with reefs, sands, and rocks in bottom. In this study area, no *in-situ* bathymetric data are available. Alternatively, the ICESat-2 bathymetric data in different dates and locations (the green trajectories in Fig. 2) were used to evaluate the bathymetric results derived from the training ICESat-2 points (the red trajectories in Fig. 2) and Sentinel-2 images.

2.2. Sentinel-2 satellite imagery

The standard Copernicus Sentinel-2A and Sentinel-2B **Level-1C** images for this study are available for free from the European Space

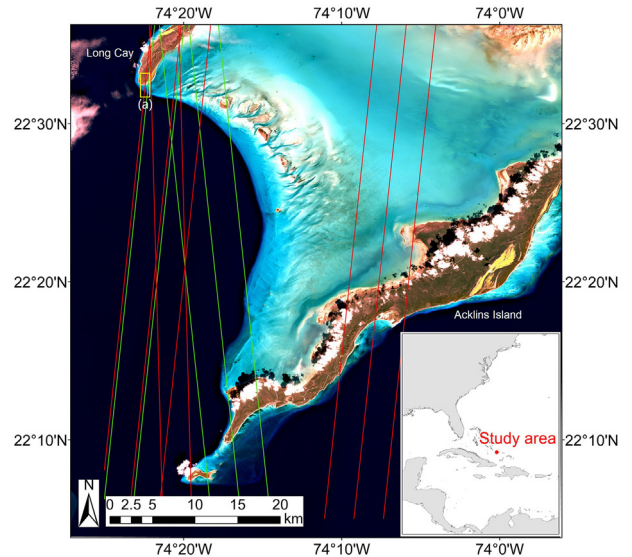


Fig. 2. ICESat-2 laser beam trajectories near the lagoon between the Acklins Island (the southeastern island) and Long Cay (the northwestern island), to the southeast of Bahama. The satellite image used as a basemap is from the Sentinel-2 imagery on 27/01/2020. Eight red lines correspond to the laser trajectories of ICESat-2 on 11/02/2019, 12/03/2019, and 02/09/2019, respectively, and they were used to train the empirical models. Five green lines correspond to the laser trajectories of ICESat-2 on 12/11/2018 and 03/06/2019, respectively, and they were used to validate the derived bathymetric results. The yellow box marked by (a) corresponds to a sampled area (to illustrate the detailed ICESat-2 photons) in Fig. 7. (For interpretation of the references to colour in this figure legend, the reader is referred to the web version of this article.)

Agency's (ESA) Sentinel Scientific Data Hub. The MultiSpectral Instrument (MSI) on board Sentinel-2 can provide high-resolution optical images for coastal and inland areas (Manzo et al., 2015). The information of the selected images for two study areas is listed in Table 1. The used images were geometrically projected with the UTM/WGS84 (Universal Transverse Mercator/World Geodetic System 84) in top-of-atmosphere reflectance. In the processing from the Level-1C to the Level-2A datasets, the used Level-1C images were atmospherically

Table 1

Detailed information on the study areas and the acquisition dates of the ICESat-2 and Sentinel-2 data.

Date/Location	Yongle Atoll	Lagoon near Acklins Island and Long Cay
	Latitude: 16.25°–16.40° N	Latitude: 22.10°–22.60° N
	Longitude: 111.30°–111.50° E	Longitude: 73.90°–74.40° W
Sentinel-2 images	24/02/2019 10/03/2020 20/03/2020 25/03/2020	06/02/2019 10/14/2019 12/23/2019 27/01/2020
ICESat-2 points (training)	22/10/2018 22/02/2019 12/04/2019	11/02/2019 12/03/2019 02/09/2019
<i>In-situ</i> measurements (validation)	Airborne bathymetric lidar (the Optech Aquarius)	ICESat-2 points on 12/11/2018 and 03/06/2019 (with different dates and locations)

corrected using the **Case 2 Regional Coast Colour processor (C2RCC)** plug-in, which is embedded in the free Sentinel Application Platform (SNAP) version 7.0.0. Comparing with the Sen2Cor (version 2.4) (that is the default Level-2A processor for the atmospheric correction and mainly designed for land areas), the C2RCC method achieved the lower root mean square differences and mean absolute differences (Casal et al., 2019; Warren et al., 2019).

The **Deglint Operator** of Sen2Cor toolbox in SNAP was used to the glint correction, which uses the NIR (Near Infrared) or SWIR (Short-wave Infrared) to estimate and correct the glint in visible wavelength bands (Hedley et al., 2005; Kay et al., 2009). The Bands 2, 3, and 4 (used in this study) were corrected using Band 8 with an identical spatial resolution of 10 m (Hedley et al., 2018). In addition, the minimal glint is virtually shown for solar zenith angles above 40° (Hedley et al., 2018). In Hedley's study, the solar zenith angles of selected test images used for the bathymetry were larger than 30° and relative azimuths were larger than 60° from direct reflectance direction. Therefore, in this study, eight Sentinel-2 MSI (Multispectral Instrument) images in two study areas were selected according to these rules to minimize the sunglint effect.

2.3. ICESat-2 lidar datasets

The ICESat-2 ATLAS has three laser beams along-track (the left, central, and right beam) and the cross-track distance between adjacent beams is 3.3 km. Each laser beam is divided into 2 sub-beams, i.e., one of them has stronger pulse energy and its energy is approximately 4 times than the other weaker sub-beam. The **ICESat-2 Level-2 ATL03 Geolocated Photons** (free from <https://search.earthdata.nasa.gov/search>) were used in this study. The L2 ATL03 datasets include all raw photons (including signal and noise photons) that were recorded in six different trajectories (three strong beams and three weak beams), and each photon has a unique latitude, longitude, and elevation based on the WGS84 ellipsoid benchmark (Neumann et al., 2019). The errors of atmospheric delay, solid tide, systematic pointing bias have been corrected in the L2 ATL03 datasets. However, the bathymetric errors, e.g., the effect of the water surface fluctuation as well as the refraction effect of sloping sea surface, water column, non-nadir incidence, and the scattering effect related to atmospheric conditions and inherent water properties, were not corrected (Jasinski et al., 2016; Li et al., 2019).

In addition, because of the sensitive detectors, the raw data photons in ATL03 datasets are very noisy (mainly due to the solar background), especially in the daytime. In ATL03 datasets, the parameter of 'confidence' is provided to classify each photon as being either likely signal or noise (Neumann et al., 2019). With a higher confidence (from 0 to 4), the photon is more likely a signal. This algorithm assumes the noise photons follow a Poisson distribution (McGill et al., 2013) and detects signal photons that are outliers to Poisson distribution. However, because of the attenuation and scattering effect in water column, the

distribution of signal and noise photons is quite different from that of atmosphere. The confidence in the ATL03 does not always perform well, i.e., many of signal photons on seafloor are discarded and many of the noise photons remain (as illustrated in the following Figs. 5, 6, and 7). Therefore, in this study, a modified density-based spatial clustering of applications with noise (DBSCAN) method was proposed to detect signal photons from the ATL03 raw data photons in place of official results (via the 'confidence' values).

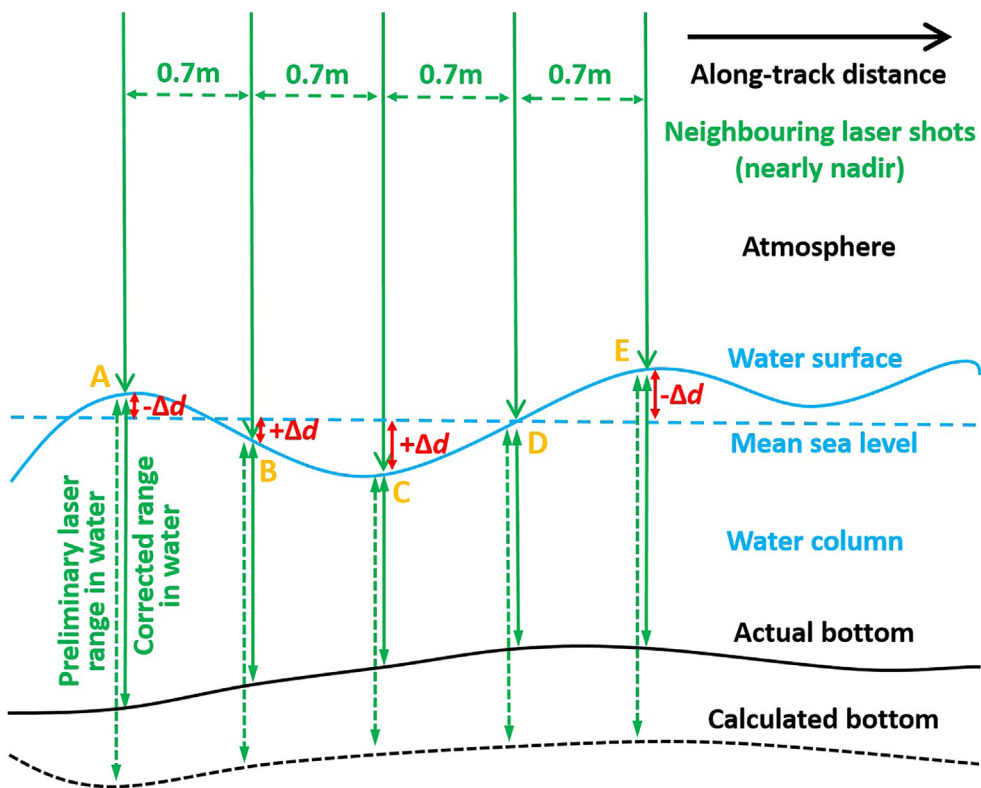
The detailed information on the study areas and the acquisition dates of the ICESat-2 and Sentinel-2 data is listed in Table 1. In each study area, four Sentinel-2 images on different dates were used to derive the bathymetric maps, which were further used to analyze the performance and consistency of this approach. In each study area, from the multi-date Sentinel-2 images, no significant difference was observed visually. In two study areas, the periods between the earliest and latest Sentinel-2 images are approximately a year. It should be noted that the OTPS2 tide model (Egbert and Erofeeva, 2002) was used for the tide correction based on the acquisition times of Sentinel-2 images and ICESat-2 points, and all SDB results were presented relative to the mean sea level (MSL).

3. Methods

3.1. Detection method for ICESat-2 signal photons

For sea-ice and forest areas, many algorithms have been developed to detect specific signal photons from raw data photons (Kwok et al., 2016; Nie et al., 2018; Popescu et al., 2018; Neuenschwander and Pitts, 2019). In our previous studies, a method was proposed to detect the ground and seafloor photons, and a joint north sea wave project (JONSWAP) wave algorithm was developed to extract the signal photons on the water surface (Ma et al., 2019; Ma et al., 2018). In coastal areas, the two methods achieved a better performance than the confidence parameters provided by the MABEL (Multiple Altimeter Beam Experimental Lidar) datasets. The airborne MABEL was designed to be a technique demonstrator for the ICESat-2 satellite photon-counting lidar. In the DBSCAN algorithm, points in a cluster are classified as signal when the point density of its neighboring points (within a given radius based on the Euclidean distance) exceeds a threshold (Ester et al., 1996), i.e., the minimum number of points (*MinPts*). The adaptive threshold *MinPts* is the key parameter in the DBSCAN algorithm.

The raw data photons in ICESat-2 datasets are different from those in the MABEL datasets. The vertical range of the MABEL datasets is normally 1500 m, whereas the ICESat-2's vertical range is only within 60 m in ocean areas. According to our previous study, the raw data photons from the MABEL datasets were divided into several segments to calculate the expected photon number of noise SN_2 within a given radius R_a and the expected photon number of signal and noise SN_1 , and then to calculate the adaptive threshold *MinPts* by Eq. (1), where M is the vertical segment (Ma et al., 2019).



$$\text{MinPts} = \frac{2SN_1 - SN_2 + \ln(M)}{\ln\left(\frac{2SN_1}{SN_2}\right)} \quad (1)$$

In this study, we modify the calculation process of *MinPts* to apply to the ICESat-2 datasets. First, the ATL03 raw data photons were used (including all photons with confidence from 0 to 4). In each ICESat-2 route that flew over the study area, every continuous 10,000 raw photons in the along-track direction were calculated together.

Second, because the vertical range is only 60 m, all photons were directly used to calculate the expected photon number of signal and noise SN_1 within a given radius R_a (expressed as Eq. (2)) rather than divide into many vertical segments, i.e., $M = 1$ in Eq. (1).

$$SN_1 = \frac{\pi R_a^2 N_1}{hl} \quad (2)$$

N_1 is the number of photons in total (including the noise and signal photons); h is the vertical range (the difference between the maximum and minimum elevations in current segment of 10,000 points); and l is the along-track range (the difference between the maximum and minimum along-track distance in current segment).

Third, the expected photon number of noise SN_2 was calculated using the photons corresponding to the lowest 5-m elevations within the vertical range because the layer in the lowest 5-m elevation is in water column and has fewer bathymetric photons.

$$SN_2 = \frac{\pi R_a^2 N_2}{h_2 l} \quad (3)$$

N_2 is the number of photons that corresponds to the lowest 5-m elevations and h_2 is the height of the 5-m lowest layer, i.e., $h_2 = 5$. Then, the adaptive threshold *MinPts* is calculated by.

$$\text{MinPts} = \frac{2SN_1 - SN_2}{\ln\left(\frac{2SN_1}{SN_2}\right)} \quad (4)$$

It should be noted that the minimum *MinPts* is 3, i.e., if the calculated *MinPts* is less than 3, it will be set to 3.

Fig. 3. Bathymetric geometry of the ICESat-2. The ICESat-2 has a 0.7 m along-track interval between adjacent laser shots. In water column, for each laser shot, the green dashed line corresponds to preliminary laser range R_p that has not corrected the refraction effect in water column; the green solid line corresponds to corrected laser range R_c that has not corrected the fluctuation effect on sea surface; and red solid line corresponds to the current water level bias Δd , which may be positive (point B and C) or negative (point A and E) or zero values (point D). (For interpretation of the references to colour in this figure legend, the reader is referred to the web version of this article.)

Finally, the radius of a neighborhood R_a is set to different values because the solar backgrounds are quite different at daytime and night. In the daytime, the raw data photons are much noisier than those at night. Hence, the radius R_a was set to 1.5 m in the daytime to avoid noise photons regarding as signal, whereas the radius R_a was 2.5 m at night to search more possible bathymetric signal photons. In every 10,000 points along-track segment, the signal photons on sea surface and seafloor were extracted from the ATL03 raw data photons by the DBSCAN calculator with the given radius R_a and adaptive threshold *MinPts*.

3.2. Bathymetric correction for seafloor photons

Parrish et al. (2019) proposed a simple and effective method to correct the refraction effect in water column, which is largest item in bathymetric errors. This classical method is based on a simplified assumption of a flat water surface, which is not appropriate for the fluctuating sea surface. In this study, we corrected the refraction error in water column, the refraction error on sloping water surface, and the error caused by the fluctuation effect on the water surface. The latter two items were implemented for the first time for a satellite photon-counting lidar. Although both studies involve the refraction error in water column, this error in our study is related to the fluctuating sea surface, i.e., the current water level of each laser pulse should be calculated as the air/water interface or the starting point when the laser enters the water column. The implementation process is different from Parrish's classical method.

The signal photons on sea surface and seafloor were detected using the above-mentioned method in last section. To obtain the precise water depth along ICESat-2's flight routes, the sea surface photons should be firstly discriminated against the seafloor photons. The local mean sea level L_m and the root mean square (RMS) wave height were calculated by the mean and standard deviation from the detected photons on the sea surface. All photons with the elevations lower than the local mean sea level minus 3-time RMS wave height were identified

as seafloor photons.

Second, to offset the effect of the water surface fluctuation and the refraction effect in water column, the corresponding along-track water depth was calculated by the ray tracing method for each laser shot. Fig. 3 illustrates the bathymetric geometry of the ICESat-2. With an approximately 500 km altitude and 10 kHz laser repetition frequency, the interval between adjacent laser pulses on Earth's surface is approximately 0.7 m in the along-track direction for the ICESat-2 (Markus et al., 2017). Using the time tag for each laser shot from the ATL03 dataset, the photons with identical time tag can be obtained. For each laser shot, the preliminary laser ranges R_p in water column for all seafloor photons were calculated by subtracting the current water level L_c from the elevation of seafloor photons (the green dashed lines in Fig. 3), where the current water level L_c is equal to the mean value of the signal photons on sea surface at the current laser shot. The corrected laser range R_c (the green solid lines in Fig. 3) was calculated by $R_c = R_p n_1 / n_2 \approx 0.75 R_p$ (Parrish et al., 2019), where n_1 is the refractive index in atmosphere (nearly equal to 1) and n_2 is the refractive index in water (nearly equal to 1.334).

Then, the water depth at each laser shot was calculated by offsetting current water level bias Δd (the red solid lines in Fig. 3) to the corrected laser range R_c . As the sea surface is fluctuating, at each point or each laser shot, the current water level bias Δd may be positive (point B and C in Fig. 3) or negative (point A and E in Fig. 3) and it is equal to the difference between the local mean sea level and current sea level, i.e., $\Delta d = L_m - L_c$. Consequently, for each laser shot, the corresponding water depth R is calculated by.

$$R = \frac{n_1 R_p}{n_2} + (L_m - L_c) \quad (5)$$

It should be noted that the water depth R has corrected the refraction effect in water column and the fluctuation effect on sea surface, but does not correct the refraction effect arising from the sea surface slope.

Hence, the refraction bias of water depth arising from the sea surface slope was corrected as follows. Assuming the ICESat-2's three beam lasers are nearly nadir incident as illustrated in Fig. 4. The incident laser penetrates the water/air interface at the point O, where corresponds to the water surface slope of θ_1 . Actually, the incidence angle is equal to the water surface slope of θ_1 . Based on the Snell's Law, the refraction angle in water column θ_2 can be expressed as $\theta_2 = \arcsin(n_1 \cdot \sin \theta_1) / n_2$. In Eq. (5), R represents the laser range in water column.

If the refraction effect arising from the water surface slope is not considered, the laser path is nadir in water column and hit the bottom at the point A, i.e., the calculated water depth is equal to R . The actual laser path is with the angle of α (the relationship is $\alpha = \theta_1 - \theta_2$) and will hit the actual bottom at the point B. The horizontal error of the refraction effect arising from the water surface slope Δx is calculated by $\Delta x = \sin \alpha \cdot R = \sin(\theta_1 - \theta_2) \cdot R$. Given that the AOB is an isosceles triangle, the angle β is equal to $\alpha/2$ or $(\theta_1 - \theta_2)/2$. The vertical error (depth error) is written as.

$$\Delta z = \tan[(\theta_1 - \theta_2)/2] \sin(\theta_1 - \theta_2) R \quad (6)$$

It should be noted that, the refraction effect arising from the sea surface slope shortens the water depth; therefore, for each laser shot, the water depth R calculated by Eq. (5) should subtract Δz to offset the refraction bias arising from the sea surface slope.

Finally, owing to the tidal effect, the local water level can vary over time. Based on the OTPS2 tide model (Egbert and Erofeeva, 2002), the differences Δh_t between the MSL and the local mean sea levels when three ICESat-2 routes flew over the study area were calculated to remove the tidal effect. In summary, for each laser shot, after the correction of the refraction effect (in water column and by sloping sea surface), the fluctuating effect on sea surface, and the tidal effect, the water depth D can be expressed as.

$$D = [1 - \tan[(\theta_1 - \theta_2)/2] \sin(\theta_1 - \theta_2)] \left[\frac{n_1 R_p}{n_2} + (L_m - L_c) \right] + \Delta h_t \quad (7)$$

3.3. SDB methods with ICESat-2 bathymetric points

Due to the historical significance, simplicity, widespread utilization, and good accuracy (Tragano et al., 2018), in this study, we applied two classical empirical models to the Sentinel-2 MSI (Multispectral Instrument) imagery, which are the same or similar to algorithms provided in Sen2Cor plug-in in ESA's SNAP toolbox (<http://step.esa.int/main/toolboxes/snap/>). With the pre-processed Sentinel-2 image including multiple bands and ICESat-2 bathymetric points (which were used as *priori* measurements to calculate the relationship), two classical empirical SDB methods (i.e., the linear band model and band ratio model) were applied to generate bathymetric maps in two study areas.

Lyzenga developed the linear band model to derive shallow water depth from multispectral imagery and updated in subsequent researches (Lyzenga, 1978, 1981; Lyzenga, 1985; Lyzenga et al., 2006). For Sentinel-2 images, this inversion model (expressed in Eq. (8)) uses the log-transformed linear multispectral bands as the predictor to calculate water depths.

$$\hat{H} = h_0 - \sum_{j=1}^N h_j R_{rsj} \quad (8)$$

\hat{H} is the bathymetry derived from the pre-processed Sentinel-2 image, R_{rsj} is the above-water surface remote sensing reflectance at j -th band of Sentinel-2 images after pre-processing, h_0 and h_j are the linear relationship constants between R_{rsj} and water depths. All values of h_0 and h_j can be obtained by minimizing the difference between the estimated depth \hat{H} and the *priori* water depths H .

The second classical SDB method is the band ratio model (Stumpf et al., 2003), which links the above-water surface remote sensing reflectance ratio of two bands to the *priori* water depths. The log-transformed relationship between the ratio of a higher-absorption band and a lower-absorption band was derived, and then a linear model can be developed between the ratio and the retrievable water depth (Stumpf et al., 2003). This model can be expressed as.

$$\hat{H} = m_1 \frac{\ln(n R_{rsi})}{\ln(n R_{rsj})} - m_0 \quad (9)$$

\hat{H} is the bathymetry derived from the pre-processed Sentinel-2 image, R_{rsi} and R_{rsj} is the above-water surface remote sensing reflectance of different wavelengths for bands i and j , and m_0 and m_1 are the offset and gain values to linearly transfer the model results to water depths, the values of m_1 and m_0 can be obtained by minimizing the difference between the estimated depth \hat{H} and the *priori* water depths H . n is a fixed coefficient, which is generally set to 1000, mainly accounting for keeping log values positive under any conditions (Stumpf et al., 2003).

4. Results

4.1. ICESat-2 bathymetric points

Using the proposed method in Section 3.1, the signal photons of each laser trajectory were first detected from the L2 ATL03 raw datasets. Near Yongle Atoll, two sampled areas where the seafloor were detected were selected to illustrate in detail in Figs. 5 and 6. The first sampled area (in Fig. 5) corresponds to the right orange box marked by (a) in Fig. 1, when the ICESat-2 flew over this area at 15:38:35 of local time on 22/10/2018. This sampled dataset was obtained in daytime, and is very noisy. The second sampled area (in Fig. 6) corresponds to the left orange box marked by (b) in Fig. 1, when the ICESat-2 flew over this area at 21:51:59 of local time on 21/02/2019. This sampled dataset was obtained at night, and has fewer noise photons. For two sampled

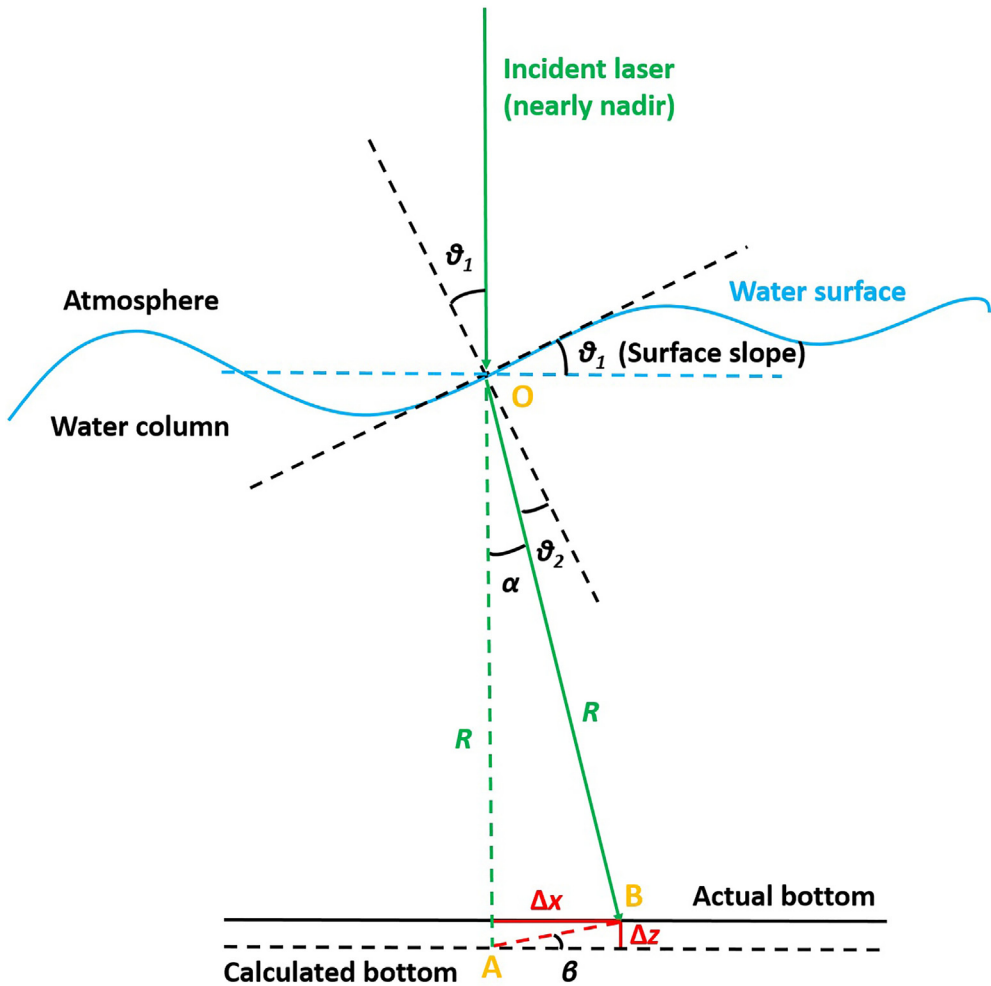


Fig. 4. Correction for the refraction bias of water depth arising from the sea surface slope. θ_1 is he incidence angle (that is almost equal to the water surface slope); θ_2 is the refraction angle in water column; R is the laser range in water column; and Δz is the refraction bias arising from the sea surface slope.

areas, Figs. 5(a) and 6(a) show the enlarged satellite image; Figs. 5(b) and 6(b) illustrate the detected signal photons from the ATL03 official results and our results; and Figs. 5(c) and 6(c) illustrate the corrected underwater photons with the bathymetric correction method.

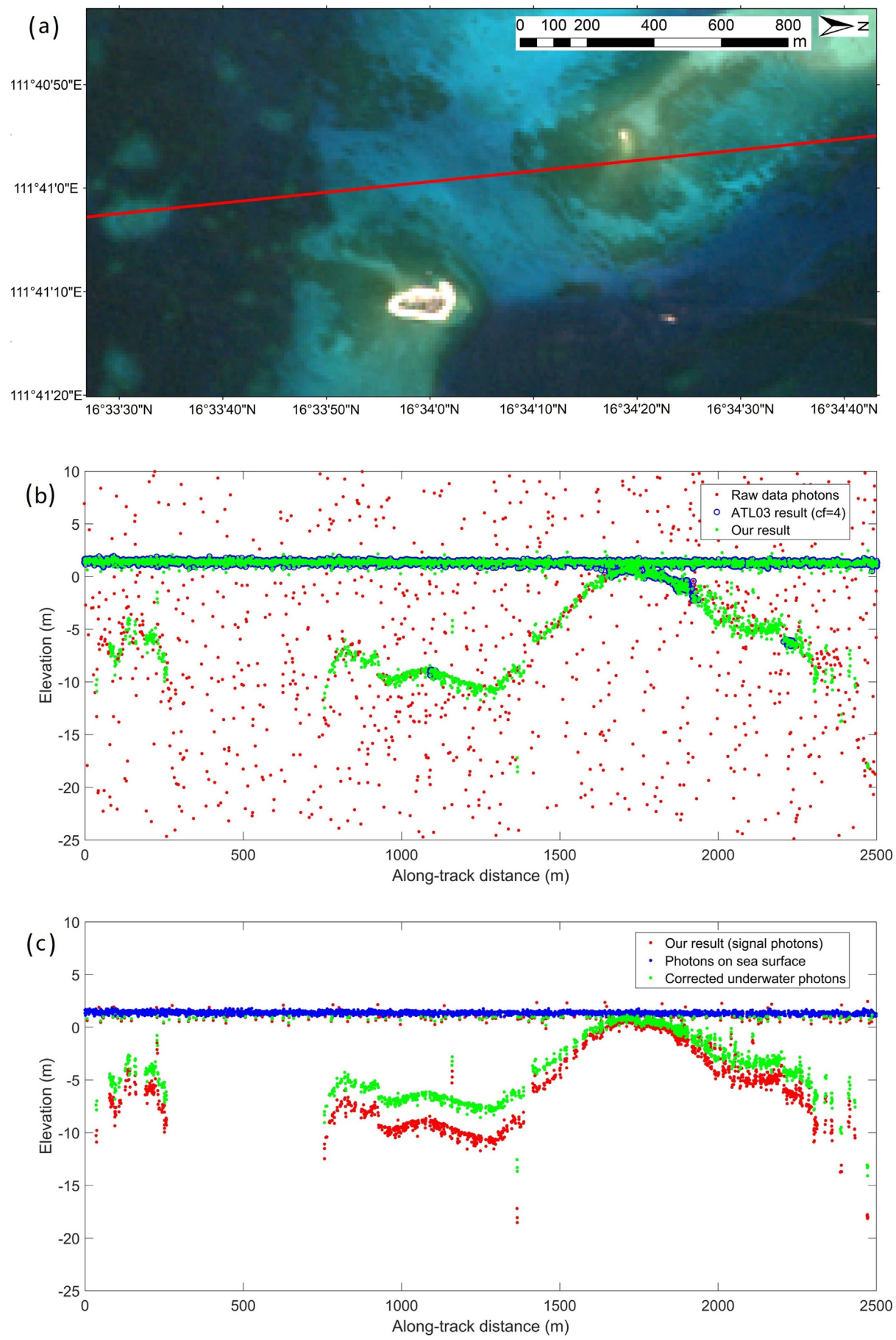
In Fig. 5(a), from south to north, the laser trajectory was first over a segment of shallow water area, flew over a segment of the deeper water area, passed away a reef area, and finally backed to the deeper water area. In our result using green points in Fig. 5(b), the detected seafloor signal photons are well in accordance with the topography reflected by the optical image, whereas the ATL03 result (with the highest ‘confidence’ of 4) fails to detect most of underwater signal photons (using blue circles, especially when the depth is beyond 5 m). In Fig. 6(a), from south to north, the laser trajectory was over a big reef. In the first half segment, the underwater topography is very rough, and it becomes relatively flat in the last half segment. Our result (using green points) also has a better performance than that of the ATL03 result. More seafloor signal photons were detected by our method and many underwater noise photons remain in the ATL03 result. As shown in Fig. 5, the raw data photons are much noisier than those captured at night in Fig. 6 (at 21:51:59) because the measured time was in daytime (at 15:38:35 of local time) when the solar-induced background noise was very strong.

Near the lagoon of Acklins Island and Long Cay, a sampled area was selected to illustrate in detail in Fig. 7, which corresponds to the yellow box marked by (a) in Fig. 2. The ICESat-2 flew over this area at 21:51:18 of local time on 11/02/2019. In Fig. 7(a), from north to south,

the laser trajectory was from Long Cay (the northwestern island in Fig. 2) into the lagoon, and then entered into the deep sea. In the first half segment in the water area, the underwater topography has a moderate slope, and the slope becomes very sharp in the last half segment. Our result (using green points) also has a better performance than that of the ATL03 result, and many underwater noise photons remain in the ATL03 result. From Figs. 5, 6, and 7, in both two study areas, our method achieves a better performance to detect the seafloor signal photons in daytime and night, which is essential to further calculate the local water depths.

In Figs. 5(b)–7(b) and Figs. 5(c)–7(c), the abscissa represents to the along-track distance of the ICESat-2's flight route, i.e., all lidar photons were transformed from the geographic latitude, longitude, and elevation to the along-track distance and elevation (in along-track coordinates), and vertical coordinate represents the elevation on the WGS84 ellipsoid benchmark. The zero of the along-track distance corresponds to the southernmost location of the flight route in Figs. 5(a)–7(a). It should be noted that the satellite images in Figs. 5(a)–7(a) are rotated 90 degrees clockwise to show the along-track distance on the horizontal axis and the elevation on the vertical axis in Figs. 5(b)–7(b) and Figs. 5(c)–7(c).

Next, the elevation of underwater photons from our results, i.e., the green points in Figs. 5(b)–7(b), was corrected by the correction method in Section 3.2. Near Yongle Atoll, in Figs. 5(c) and 6(c), photons on sea surface (using blue circles) were identified to calculate the local water level and RMS wave height, which were then used to determine the



(caption on next page)

Fig. 5. Sampled area near Yongle Atoll locates in the right orange box marked by (a) in Fig. 1, when ICESat-2 flew over this area at 15:38:35 of local time on 22/10/2018. The top sub-figure (a) shows the enlarged satellite image; the middle sub-figure (b) illustrates the detected signal photons from the ATL03 official results and our results; and the bottom sub-figure (c) illustrates the corrected underwater photons from our result photons, i.e., the green points in (b). (For interpretation of the references to colour in this figure legend, the reader is referred to the web version of this article.)

elevation threshold to classify the underwater photons. In Fig. 5, on 22/10/2018, the local water level was 1.36 m and the RMS wave height was 0.14 m. In Fig. 6, on 22/02/2019, the local water level was 1.66 m and the RMS wave height was 0.14 m. Given that the RMS wave height was 0.14 m, if the water surface fluctuation was not corrected, the same level error would introduce to the bathymetric results. For each laser shot, the refraction effect in water column was corrected by Eq. (5). Similarly, near the lagoon of Acklins Island and Long Cay, in Fig. 7, on 11/02/2019, the local water level was −35.32 m and the RMS wave height was 0.17 m. In Fig. 7(c), the underwater photons were corrected for the refraction effect in water column for each laser shot. A 0.14–0.17 m RMS wave height corresponds to 1 sigma, i.e., wave heights in local areas can be up to over 0.5 m; therefore, the fluctuation effect on the water surface should be considered and corrected.

Near Yongle Atoll, in Figs. 5 and 6, the mean water surface slopes were approximately 0.16 and 0.14 (i.e., $\theta_1 = 9.2^\circ$ and 8.0°) respectively, which were calculated by the neighboring laser points on the water surface. Similarly, near the lagoon of Acklins Island and Long Cay, in Fig. 7, the mean water surface slope was approximately 0.19 (i.e., $\theta_1 = 10.9^\circ$). Therefore, the horizontal error can be expressed $0.04R$ and the vertical error in Eq. (6) is $0.0008R$ for simplicity. Because the angle α is small (less than 2.5°), the water depth can be approximately in place of the laser range R in Eq. (6). If the water depth is 20 m, the horizontal error will be 80 cm (more than 10 times arising from the non-nadir incidence) while the vertical error will be 1.6 cm. For a 17-m footprint size of the ICESat-2, the 80-cm horizontal error and the 1.6-cm vertical error can be neglected. For each laser shot, considering the local tidal effect, the along-track water depth D was calculated using Eq. (7). Finally, the corrected underwater photons are illustrated using green points in Figs. 5(c) and 6(c) near Yongle Atoll and in Fig. 7(c) near the lagoon of Acklins Island and Long Cay, respectively. In addition, a few underwater noise photons, e.g., in Figs. 5(c) and 7(c), were removed manually.

Near Yongle Atoll, it can be seen from Fig. 6(c) that the detected seafloor photons are up to water depth of ∼20 m. Near the lagoon of Acklins Island and Long Cay, in Fig. 7(c), the detected seafloor photons are up to water depth of ∼25 m. The local time in Fig. 6 when the ICESat-2 flew over Yongle Atoll is very close to that in Fig. 7 near the lagoon of Acklins Island and Long Cay (the local time is very close to 22:00 AM). The maximum bathymetric depth near the lagoon of Acklins Island and Long Cay is 5 m larger than that near Yongle Atoll.

4.2. Multispectral imagery derived bathymetry with ICESat-2 priori points

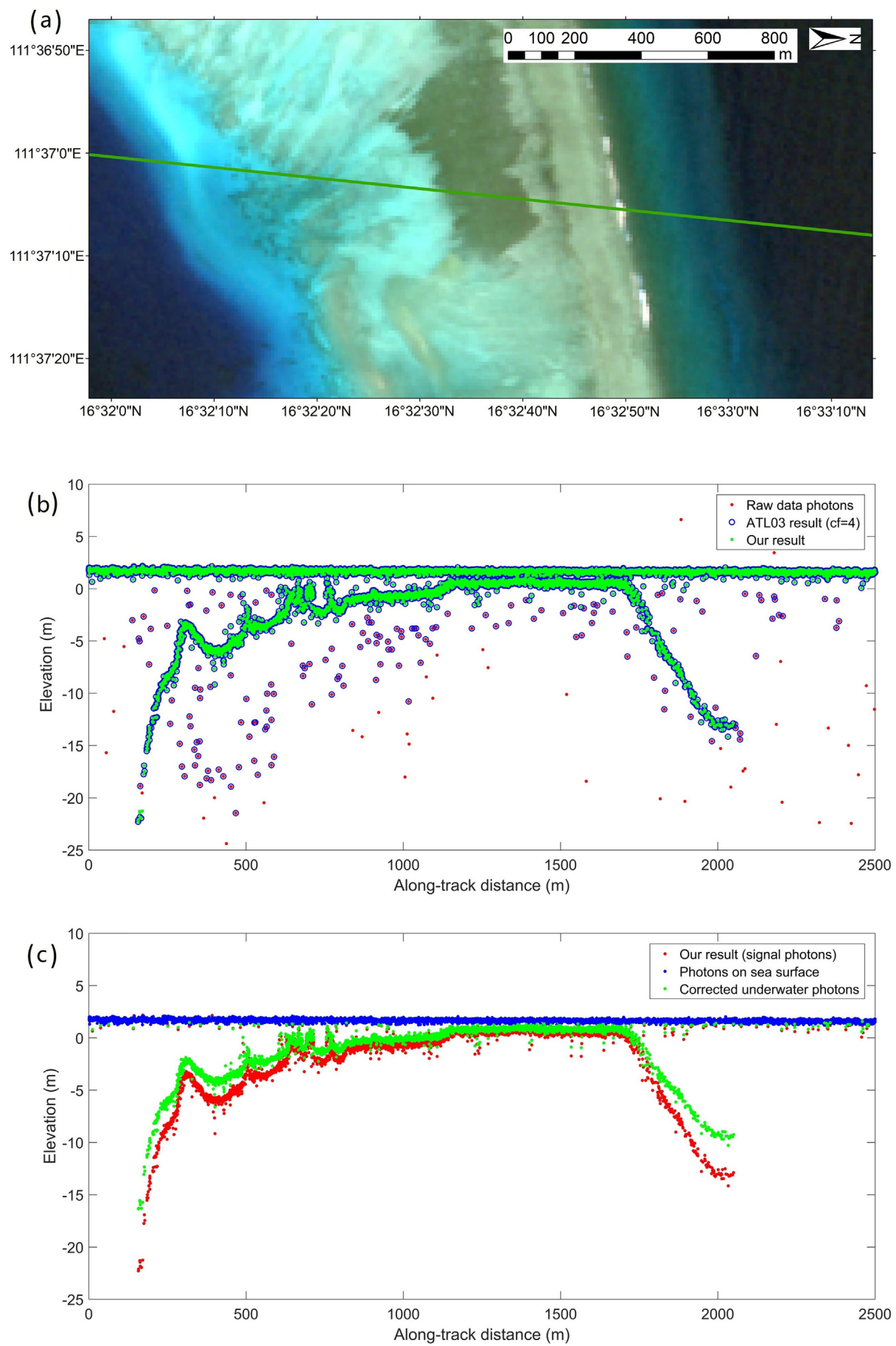
In the first study area, near Yongle Atoll, the detected ICESat-2 bathymetric points and the pre-processed Sentinel-2 images were used to train the linear band model (Eq. (8)) and the band ratio model (Eq. (9)) for each date. The gross errors were discarded according to the 3-sigma criteria; and then, the linear band model and the band ratio model were re-trained. Fig. 8 illustrates the training comparisons of the linear band models and band ratio models for the four dates of the Sentinel-2 multispectral imagery. The red line is the 1:1 line, and the blue line corresponds to the regression line. The numbers of used training bathymetric points N from the ICESat-2 data are slightly different in four dates because some gross errors were discarded. The regression equations of different models for each date are involved in Fig. 8. In addition, although the maximum bathymetric depth from the ICESat-2 near Yongle Atoll is approximately 20 m, less than 1% of the total ICESat-2 bathymetric points exceed 18 m. Therefore, the maximum water depth of the two models was set to 18 m.

In Fig. 8, for satellite images acquired on four dates and the linear band model, the R^2 are from 0.95 to 0.97 with a mean of 0.96, and the training RMSE (Root Mean Squared Error) are from 0.96 m to 1.23 m with a mean of 1.08 m. For the band ratio model, the R^2 are from 0.93 to 0.95 with a mean of 0.94, and the training RMSE are from 1.17 m to 1.41 m with a mean of 1.30 m. Generally, near Yongle Atoll, the linear band model achieves slightly better training results compared to the band ratio model.

Next, using the trained linear band model and band ratio model, and the pre-processed Sentinel-2 image for each date, the shallow water bathymetric maps near Yongle Atoll were generated and drawn in Fig. 9. Fig. 9(a)–(d) correspond to the bathymetric maps derived from the linear band models on 24/02/2019, 10/03/2020, 20/03/2020, and 25/03/2020, respectively. Fig. 9(e)–(h) correspond to the bathymetric maps derived from the band ratio models on four dates. Then, the bathymetric maps derived from the two empirical models near Ganquan Island (in the purple box in Fig. 1) were validated by the *in-situ* data captured by an airborne Optech Aquarius lidar system. The topography variation between the time when the airborne lidar surveyed and the time when the ICESat-2 and Sentinel-2 flew over this area was not considered because few constructions were made around this island in recent years.

Figs. 10 and 11 show the comparison results between the retrieved depths and *in-situ* depths near Ganquan Island, Yongle Atoll. In Fig. 10, spatial distributions of the Sentinel-2 imagery (captured on 24/02/2019 in Fig. 10(a)), the *in-situ* Optech Aquarius lidar points (in Fig. 10(f)), and derived bathymetric maps near Ganquan Island were illustrated in sequence. Fig. 10(b)–(e) correspond to the SDB maps derived from the linear band models on 24/02/2019, 10/03/2020, 20/03/2020, and 25/03/2020 respectively, and Fig. 10(g)–(j) correspond to SDB maps derived from the band ratio models on four dates. It should be noted that on different dates, due to some rocks out of the water surface, clouds, and shadows, the derived bathymetric maps may have blank areas in Fig. 9 (the entire maps near Yongle Atoll) and Fig. 10 (the enlarged maps near Ganquan Island). To further verify the accuracy of the estimation results, the error scatter diagram, R^2 , RMSE, the regression line, and the regression equation between the retrieved water depths and *in-situ* depths near Ganquan Island were illustrated in Fig. 11 on four dates. For the linear band models, the error scatter diagrams in Fig. 11(a)–(d) correspond to the maps in Fig. 10(b)–(e). For the band ratio models, the error scatter diagrams in Fig. 11(e)–(h) correspond to the maps in Fig. 10(g)–(j). The SDB maps from linear band models and band ratio models were generally well estimated (with four-date mean R^2 of 0.91 and 0.85, and four-date mean RMSE of 1.44 m and 1.85 m, respectively).

Near the lagoon of Acklins Island and Long Cay, the similar training and validation procedures were repeated. Although the maximum bathymetric depth from the ICESat-2 near Acklins Island and Long Cay is approximately 25 m, less than 1% of the total ICESat-2 bathymetric points exceed 22 m. Therefore, the maximum water depth of the two models was set to 22 m. It should be noted that the training ICESat-2 points correspond to the red lines in Fig. 2 and were captured on 11/02/2019, 12/03/2019, and 02/09/2019, and the validation ICESat-2 points correspond to the green lines were captured on 12/11/2018 and 03/06/2019. Fig. 12 illustrated the training results of the two models in detail. Fig. 12(a)–(d) correspond to linear band models on 06/02/2019, 10/14/2019, 12/23/2019, and 27/01/2020, respectively, Fig. 12(e)–(h) correspond to the band ratio models on four dates. In the training procedure, for satellite images acquired on four dates and the linear band model, the mean R^2 is 0.93 and the training mean RMSE is



(caption on next page)

Fig. 6. Sampled area near Yongle Atoll locates in the left orange box marked by (b) in Fig. 1, when ICESat-2 flew over this area at 21:51:59 of local time on 22/02/2019. The top sub-figure (a) shows the enlarged satellite image; the middle sub-figure (b) illustrates the detected signal photons from the ATL03 official results and our results; and the bottom sub-figure (c) illustrates the corrected underwater photons from our result photons, i.e., the green points in (b). (For interpretation of the references to colour in this figure legend, the reader is referred to the web version of this article.)

0.63 m. For the band ratio model, the mean R^2 is 0.93 and the training mean RMSE is 0.52 m.

The shallow water bathymetric maps near Acklins Island and Long Cay were generated and drawn in Fig. 13, where Fig. 13(a)–(d) correspond to maps derived from linear band models on four dates and Figs. 13(e)–12(h) correspond to the maps from band ratio models. The error scatter diagram, R^2 , RMSE, the regression line, and the regression equation between the retrieved water depths and *in-situ* depths near Acklins Island and Long Cay were illustrated in Fig. 14 on four dates. Generally, near Acklins Island and Long Cay, the SDB maps from linear band models and band ratio models were well estimated (with four-date mean R^2 of 0.90 and 0.89, and four-date mean RMSE of 1.18 m and 1.24 m, respectively).

5. Discussions

5.1. Consistency analysis using multi-date satellite images

To verify the spatial-temporal consistency of this approach, for each study area and each model, we calculated the mean of the four-date bathymetric maps, which was further compared with the corresponding single-date bathymetric map. Fig. 15 illustrates the spatial difference distributions between the mean of four-date bathymetric maps and single-date bathymetric map near Yongle Atoll. To be specific, Fig. 15(a)–(d) correspond to the spatial difference distributions of the linear band models on 24/02/2019, 10/03/2020, 20/03/2020, and 25/03/2020, respectively; and Fig. 15(e)–(h) correspond to the spatial difference distributions of band ratio models on four dates. For each date, the R^2 , RMSE, and bias of its spatial difference distribution were calculated. It should be noted that the R^2 , RMSE, and bias here do not represent the accuracy, but refer to the consistency when using different Sentinel-2 images and identical ICESat-2 points. Near Yongle Atoll, the mean R^2 of four-date spatial difference distributions were 0.97 and 0.95 for the linear band model and band ratio model, respectively; and the mean RMSE were 0.77 m and 0.87 m for the two models.

Similarly, near the lagoon of Acklins Island and Long Cay, the mean of the four-date bathymetric maps was calculated and further compared with the corresponding single-date bathymetric map. Fig. 16(a)–(d) illustrate the spatial difference distributions of the linear band models on 06/02/2019, 10/14/2019, 12/23/2019, and 27/01/2020, respectively; and Fig. 16(e)–(h) correspond to the spatial difference distributions of band ratio models on four dates. Near Acklins Island and Long Cay, the mean R^2 of four-date spatial difference distributions were 0.98 and 0.97 for the linear band model and band ratio model, respectively; and the mean RMSE were 0.35 m and 0.48 m for the two models.

It should be noted that the possible temporal changes of underwater topography during the period of the four-date satellite images can introduce impacts on the spatial difference distributions, the R^2 , and RMSE. Fortunately, the two study areas are very remote where the effect of human activities is relatively weak, but other factors (such as the hydrodynamic seasonality, tropical cyclone and ocean current) may have potential influences on the water depth or under underwater topography. From the multi-date Sentinel-2 images, no significant difference was observed visually. Generally, the consistency is well in two study areas and for two empirical models. The consistency near Acklins Island and Long Cay is slightly better than that near Yongle Atoll. In addition, the bias values among different dates may probably be caused by the residuals of the tidal correction.

5.2. Comparisons of linear band model and band ratio model

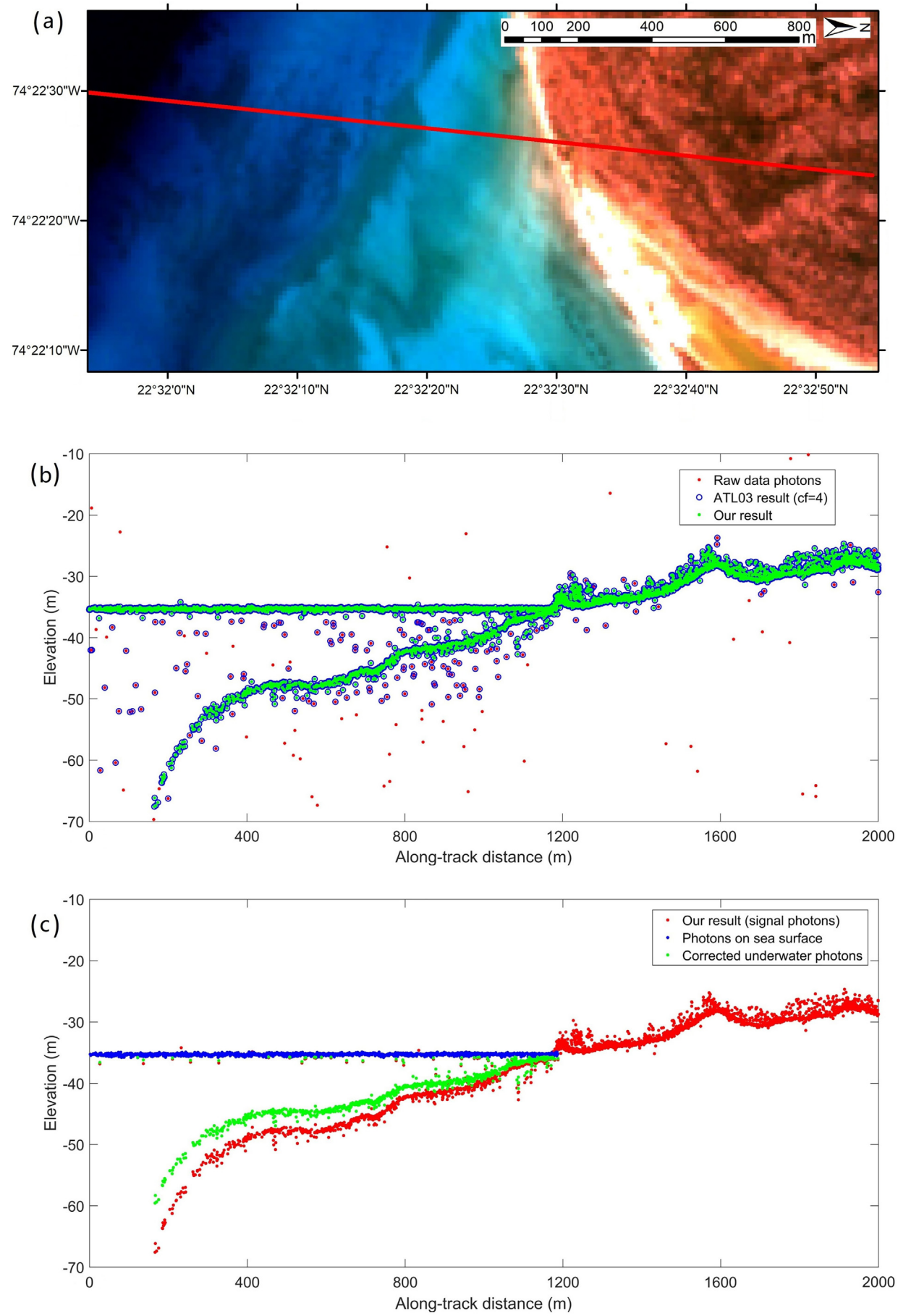
To compare the performance of the linear band models and band ratio models in two study areas, Table 2 lists the detailed information on key parameters (i.e., the R^2 and RMSE) in the procedure of the training, validation, and consistency analysis for the separate results and the mean results from four-date satellite images. In the procedures of the training, validation, and consistency analysis for both two study areas, most of the key parameters of the linear band models are slightly better than that of the band ratio models. In two study areas, the linear band models have a slightly better bathymetric accuracy in terms of RMSEs, which are less than 10% of the maximum depths. The bathymetric consistency of the linear models is also slightly better than that of the band ratio models. The reason may be that three bands of the Sentinel-2 were used for the linear models, whereas only two bands were used to produce the band ratio models (Misra et al., 2018).

5.3. Comparisons of results in two study areas

From Table 2, for both two empirical models, all key parameters (i.e., the R^2 and RMSE) near Acklins Island and Long Cay are slightly better than that near Yongle Atoll. The potential reasons are discussed as follows. (1) Near Acklins Island and Long Cay, both the training and validation *in-situ* measurements were from the ICESat-2, but the validation ICESat-2 points were captured in different dates and locations (as illustrated in Fig. 2 and shown Table 1). Near Yongle Atoll, the *in-situ* validation data were provided by the airborne Optech Aquarius lidar. Although these airborne lidar data have been proved to exhibit an accuracy of approximately 35 cm, they were captured in late 2012, whereas the Sentinel-2 images were captured from 2019 and 2020. Tiny underwater topographic changes are inevitable, which will definitely introduce errors in the validation process. (2) The variability of water quality conditions, such as the turbidity and Chlorophyll, may have impacts on bathymetry performance in different regions (Caballero et al., 2019; Caballero and Stumpf, 2019). In this study, near Yongle Atoll, in the South China Sea, the ICESat-2 lidar captured 20 m water depths and the SDB maps were generated to the depth of 18 m. Near Acklins Island and Long Cay, to the southeast of Bahama, the ICESat-2 lidar captured 25 m water depths and the SDB maps were generated to the depth of 22 m.

5.4. ICESat-2 raw data processing procedure

When processing the ICESat-2 L2 ATL03 raw data photons, the DBSCAN method was used to discard the outliers before the bathymetric correction. The main reasons of this operation are detailed as follows. (1) The bathymetric correction includes the errors arising from the refraction effect in water column and on the water surface and the error caused by the fluctuation effect on dynamic water surface. To correct these geometric errors, the signal photons on the water surface have to be firstly detected from the raw noisy photons because the refraction effect on the water surface and the fluctuation effect on the water surface both rely on the profile of local water surface. (2) The pulse width of the ICESat-2 transmitted laser is only 1.5 ns (Markus et al., 2017). Although the pulse width will be broadened in the laser transmission path, the received pulse is normally several nanoseconds. Therefore, for each laser shot, the return laser signal photons (from the water surface and underwater bottom) concentrate upon a very narrow time duration. The noise photons (i.e., outliers) that were mainly arising from the solar radiation and scattering effect are generally



(caption on next page)

Fig. 7. Sampled area near the lagoon of Acklins Island and Long Cay locates in the yellow box marked by (a) in Fig. 2, when ICESat-2 flew over this area at 21:51:18 of local time on 11/02/2019. The top sub-figure (a) shows the enlarged satellite image; the middle sub-figure (b) illustrates the detected signal photons from the ATL03 official results and our results; and the bottom sub-figure (c) illustrates the corrected underwater photons from our result photons, i.e., the green points in (b). (For interpretation of the references to colour in this figure legend, the reader is referred to the web version of this article.)

loosely distributed. The distribution of signal photons is quite different from that of the noise photons, by which the DBSCAN algorithm was designed to discard the noise photons. (3) The time bin of the PMT (photomultiplier tube) detector used in the ICESat-2 photon-counting lidar is 200 ps, and this narrow time span corresponds to only 3 cm in laser ranging in atmosphere and approximately 2.25 cm in water, which means for each laser shot, only the neighboring segment of 2.25 cm in vertical or depth direction have an effect on the return photons. With a very short width of the laser pulse and an extreme short time bin of the PMT detector, the noise photons (outliers) can be assumed to have no impact on the signal photons. (4) In addition, the bathymetric correction was implemented for every laser shot. The number of the noise photons is normally larger than that of the signal photons because the noise photons locates within the entire range gate of the ICESat-2 photon-counting lidar while the signal photons only concentrate upon a narrow vertical segment. Consequently, if the noise photons were not discarded in advance, it would cost much more computing time.

5.5. Accuracy estimation of ICESat-2 bathymetry

It is a pity that the airborne *in-situ* measurements did not cover any laser trajectories of the ICESat-2 near Ganquan Island. Thus, we used an indirect way to estimate the ICESat-2 bathymetric accuracy after the data correction in this study. From the classical study by Parrish et al. (2019), in relatively calm water area, the sea surface was assumed as a flat surface, where the bathymetric RMSE of the ICESat-2 lidar was estimated from 0.43 m to 0.60 m after correcting the refraction effect in water column (which is the largest item among bathymetric errors). Our study further corrected the fluctuation effect on the water surface and the refraction effect on the water surface, which are approximately 0.2 m in total in the study areas. Consequently, it was estimated that the bathymetric RMSE of the ICESat-2 lidar in this study was better than 0.5 m.

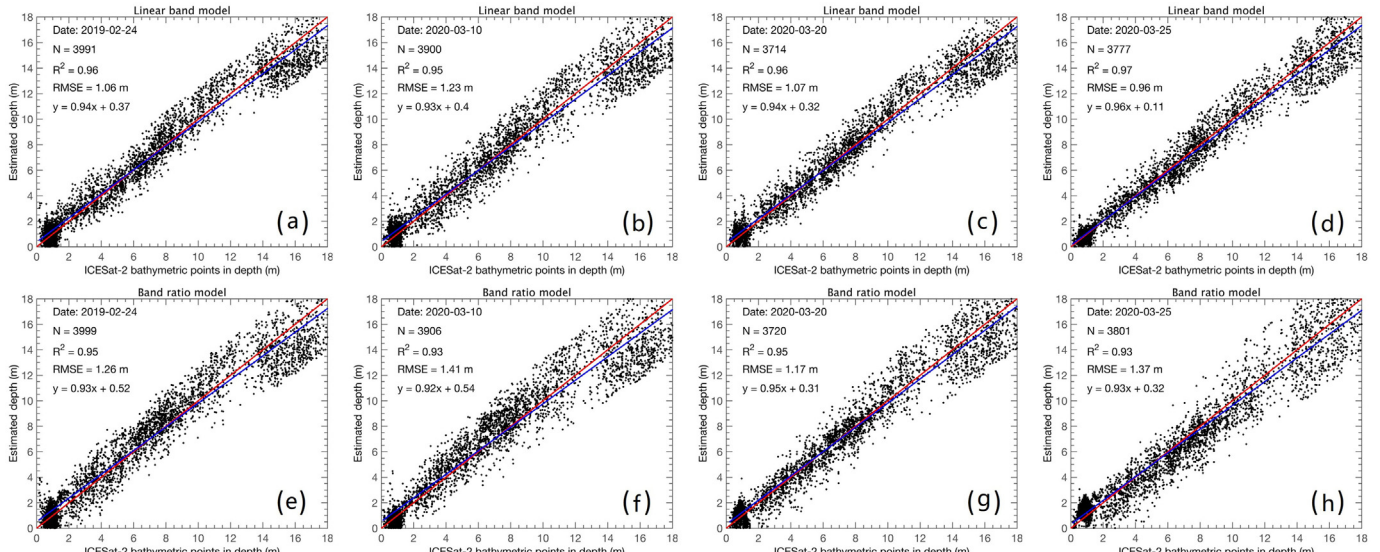
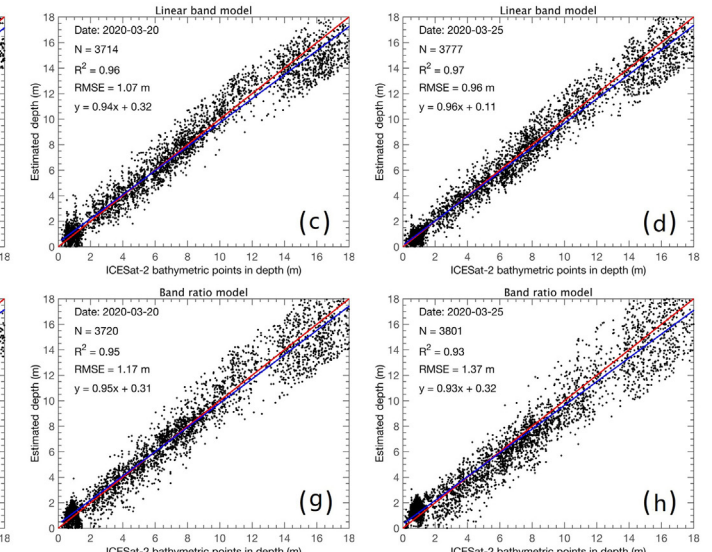


Fig. 8. Training comparisons of the linear band model and band ratio model by inputting the detected ICESat-2 bathymetric points into the pre-processed Sentinel-2 images acquired on four dates near Yongle Atoll. (a) The linear band models on 24/02/2019, (b) on 10/03/2020, (c) on 20/03/2020, and (d) on 25/03/2020, respectively; (e) the band ratio models on 24/02/2019, (f) on 10/03/2020, (g) on 20/03/2020, and (h) on 25/03/2020, respectively. The red line is the 1:1 line, whereas the blue line corresponds to the regression line. N is the number of used training bathymetric points from the ICESat-2 data after the 3-sigma filter and the regression equations of different models for each date are involved. (For interpretation of the references to colour in this figure legend, the reader is referred to the web version of this article.)

In addition, according to Neuenschwander and Magruder's study (Neuenschwander and Magruder, 2019), the horizontal RMSE on Earth's surface is approximately 5 m, i.e., the laser footprint on sea surface has a similar accuracy. When the laser pulse enters the water column, the main horizontal error is arising from the refraction effect on sloping water surface (Su et al., 2020). As shown in Fig. 4, the horizontal error from sloping water surface Δx was calculated by $\Delta x = \sin\alpha R = \sin(\theta_1 - \theta_2)R$. The incidence angle is equal to the water surface slope of θ_1 and the refraction angle in water column θ_2 can be expressed as $\theta_2 = \arcsin(n_1 \sin\theta_1)/n_2$ based on the Snell's Law. n_1 is the refractive index in atmosphere (nearly equal to 1) and n_2 is the refractive index in water (nearly equal to 1.334). The sea surface slope θ_1 is mainly related to the wind speed and the distribution can be expressed as $s^2 = 0.003 + 0.00512 U_{12.5}$ based on the Cox-Munk model (Cox and Munk, 1954), where s^2 is the surface slope variance and $U_{12.5}$ is the wind speed at 12.5 m height above the water surface. If the water depth is 15 m (R can be approximate to the water depth), the wind speed $U_{12.5}$ is 5 m/s, and the standard deviation of the surface slope is used as the surface slope, the horizontal error is less than 1 m. Considering other horizontal errors in water column, it can be estimated that the horizontal RMSE on underwater bottom of the ICESat-2 is approximately 6 m.

5.6. SDB error analysis

In this study, the errors in empirical bathymetry models are related to the Sentinel-2 images, ICESat-2 points, the 'truth' data from the airborne Optech Aquarius lidar. For Sentinel-2 images, the atmospheric correction during image pre-processing is extremely important for reliable bathymetric estimation with the Sentinel-2 (Hedley et al., 2018; Casal et al., 2019) and uncertainties of SDB results are influenced by the impact of the residual (Kutser et al., 2018; Caballero et al., 2019). The effect of the sun glint and white-caps can seriously influence the



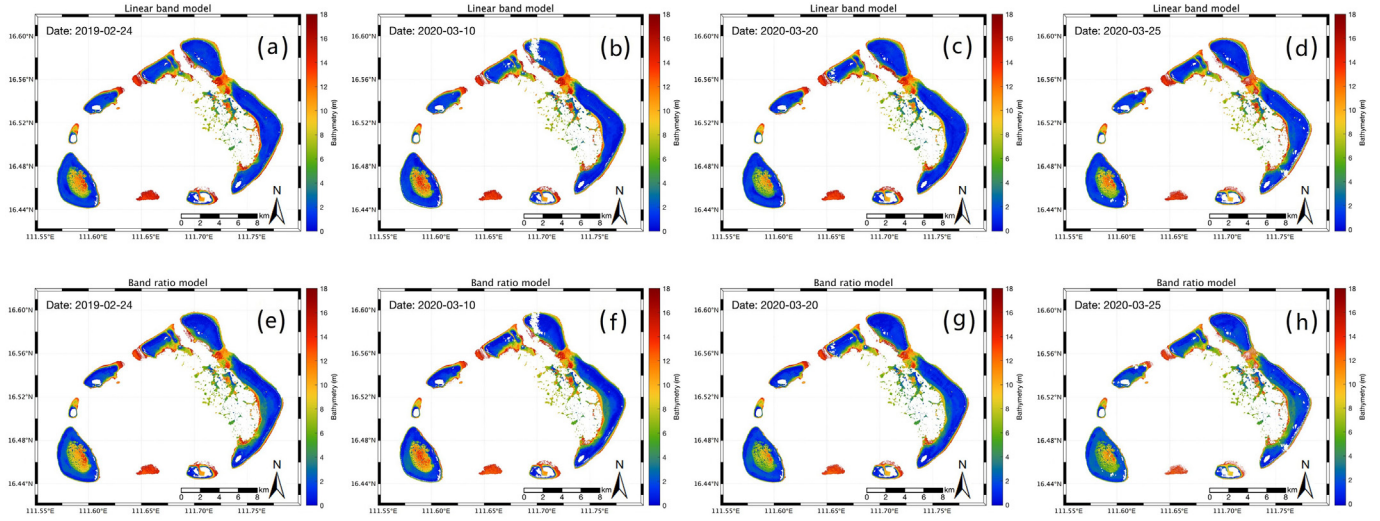


Fig. 9. Shallow water bathymetric maps derived from the two models for Yongle Atoll using multi-date satellite images. (a) The linear band models on 24/02/2019, (b) on 10/03/2020, (c) on 20/03/2020, and (d) on 25/03/2020, respectively; (e) the band ratio models on 24/02/2019, (f) on 10/03/2020, (g) on 20/03/2020, and (h) on 25/03/2020, respectively. Note that land areas (over the water level), clouds covered areas, and water depths deeper than 18 m were subtracted in maps.

reflectance (up to 30%) in the measurement of water depths (Kay et al., 2009). Although the sun glint effect was corrected by the Deglint Operator in Sen2Cor. The residuals cannot be neglected and will introduce error to the water depth (Hedley et al., 2005).

Many studies indicated that the accuracy of the satellite-derived bathymetry can be influenced by the local water transparency, water column conditions and bottom types at the time when the image was acquired (Casal et al., 2020; Lafon et al., 2002; Vahtmae and Kutser, 2016; Caballero and Stumpf, 2019). The prediction accuracy is related to how well the *in-situ* measurements covering all bottom types and

water quality conditions (Monteys et al., 2015; Casal et al., 2019). For the ICESat-2 datasets, although most errors have been corrected, the bathymetric data are also influenced by the scattering effect in water column (up to many centimeters) (Su et al., 2020). The *in-situ* validation data from the airborne Optech Aquarius lidar have an accuracy of approximately 35 cm but are a bit outdated to the acquisition dates of the Sentinel-2 and ICESat-2 data (Su et al., 2020). Meanwhile, the validation process (matching the image pixels with the *in-situ* bathymetric points) can also introduce error due to the spatial resolution and geolocation, especially when the seafloor has higher slope or roughness. In

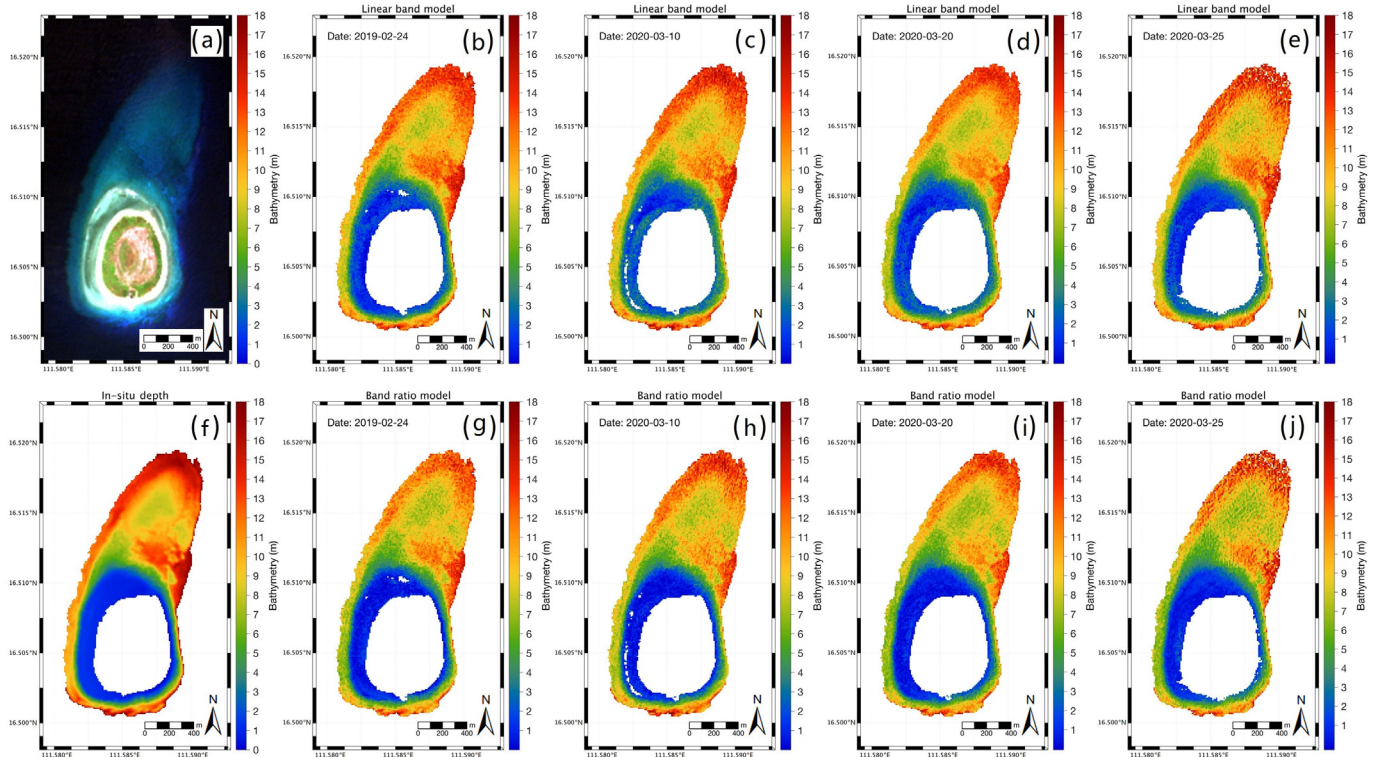


Fig. 10. Spatial distributions of the Sentinel-2 imagery, Optech Aquarius lidar datasets, and derived bathymetric maps near Ganquan Island, Yongle Atoll. (a) Sentinel-2 imagery on 24/02/2019 image of Ganquan Island; (b)-(e) SDB maps derived from the linear band model on 24/02/2019, 10/03/2020, 20/03/2020, and 25/03/2020, respectively. (f) *In-situ* truth data from the airborne Optech Aquarius bathymetric lidar. (g)-(j) SDB maps derived from the band ratio model on 24/02/2019, 10/03/2020, 20/03/2020, and 25/03/2020, respectively.

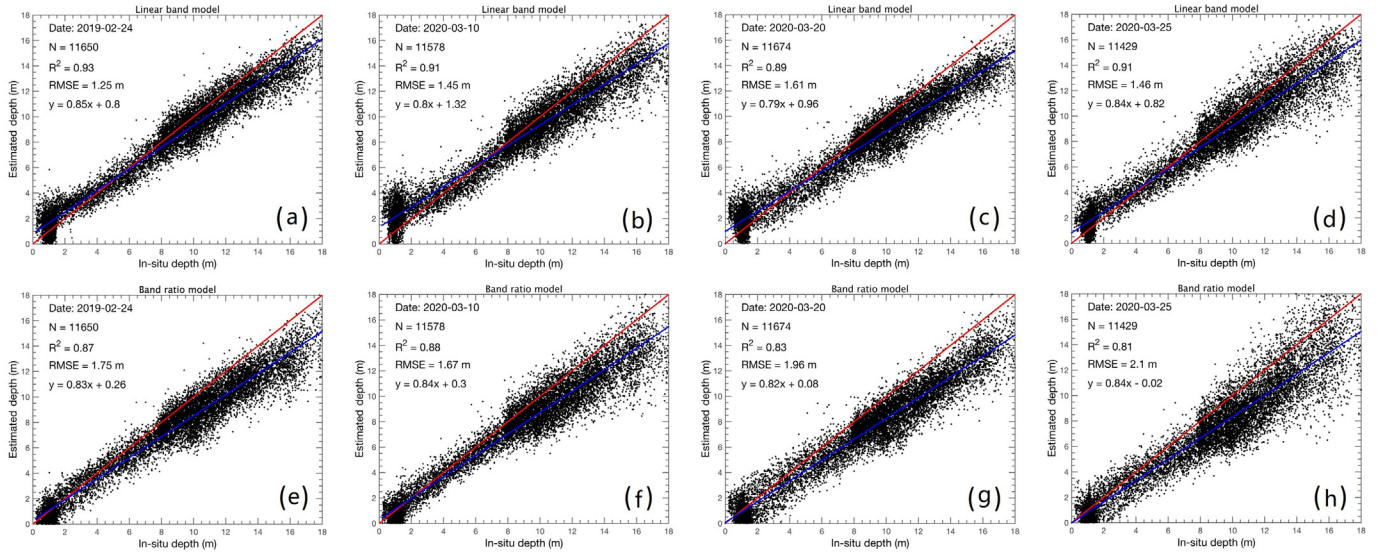


Fig. 11. Error scatter diagrams of retrieved water depths and *in-situ* depths near Ganquan Island, Yongle Atoll on four dates. (a) The linear band models on 24/02/2019, (b) on 10/03/2020, (c) on 20/03/2020, and (d) on 25/03/2020, respectively; (e) the band ratio models on 24/02/2019, (f) on 10/03/2020, (g) on 20/03/2020, and (h) on 25/03/2020, respectively. The red line is the 1:1 line near Ganquan Island, whereas the blue line corresponds to the regression line. N is the number of *in-situ* bathymetric points from the airborne Optech Aquarius lidar that were used to validate the derived bathymetric maps near Ganquan Island. The regression equations of different models for each date are also involved. (For interpretation of the references to colour in this figure legend, the reader is referred to the web version of this article.)

addition, tidal conditions could also have small impact on the accuracy of SDB results (Caballero and Stumpf, 2019).

6. Conclusions

In this study, the bathymetric points from the spaceborne ICESat-2 lidar were used in place of the *in-situ* auxiliary bathymetric points to train the classical empirical models (i.e., the linear model and the band ratio model). Using this new approach, the bathymetric map in shallow waters can be produced with only satellite remotely sensed data via empirical models (based on the new ICESat-2 lidar data and the

Sentinel-2 multispectral imagery). First, an improved DBSCAN method was proposed to detect the bathymetric signal points from the noisy raw ICESat-2 data photons. Compared to the official results of the bathymetric signal photons, the DBSCAN method performs much better in daytime and at night. Second, for the first time, the bathymetric errors caused by the refraction effect in water column, the refraction effect on the water surface, and the fluctuation effect on the water surface were analyzed and corrected for the ICESat-2 datasets. Third, in two study areas (near Yongle Atoll and near Acklins Island and Long Cay), the ICESat-2 bathymetric points were used as the *priori* measurement to train the local linear band models and the band ratio models with the

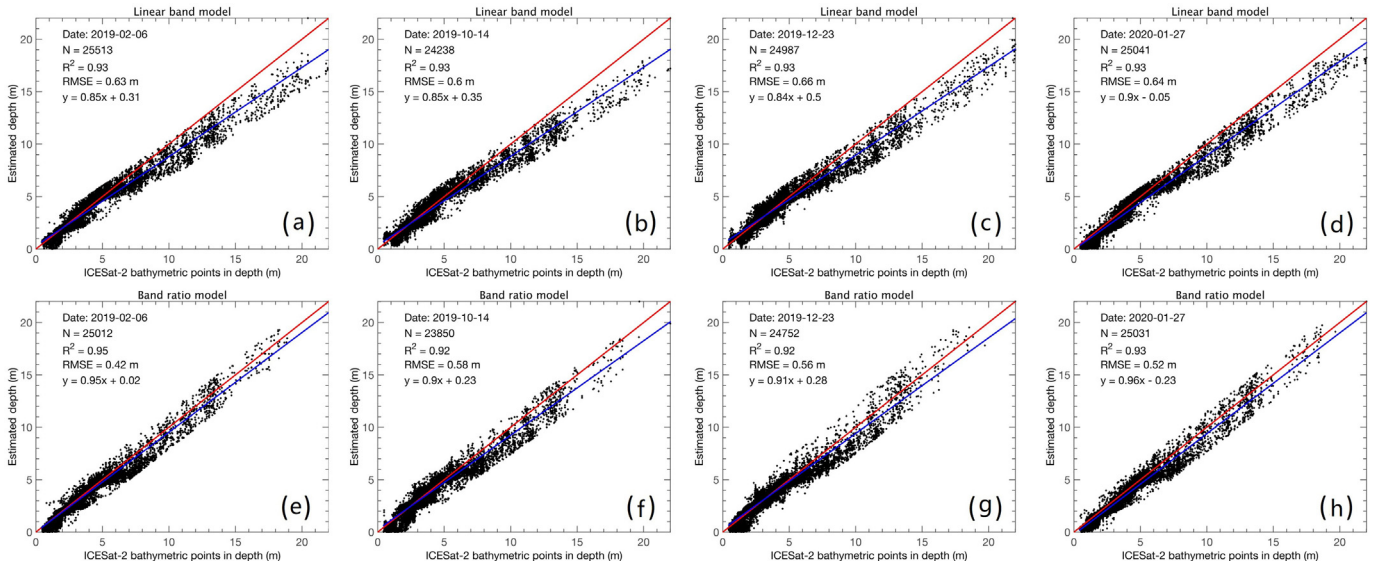


Fig. 12. Training comparisons of the linear band model and band ratio model by inputting the detected ICESat-2 bathymetric points (corresponding to the red lines in Fig. 2) into the pre-processed Sentinel-2 images acquired on four dates near Acklins Island and Long Cay. (a) The linear band models on 06/02/2019, (b) on 10/14/2019, (c) on 12/23/2019, and (d) on 27/01/2020, respectively; (e) the band ratio models on 06/02/2019, (f) on 10/14/2019, (g) on 12/23/2019, and (h) on 27/01/2020, respectively. The red line is the 1:1 line, whereas the blue line corresponds to the regression line. N is the number of used training bathymetric points from the ICESat-2 data after the 3-sigma filter and the regression equations of different models for each date are involved. (For interpretation of the references to colour in this figure legend, the reader is referred to the web version of this article.)

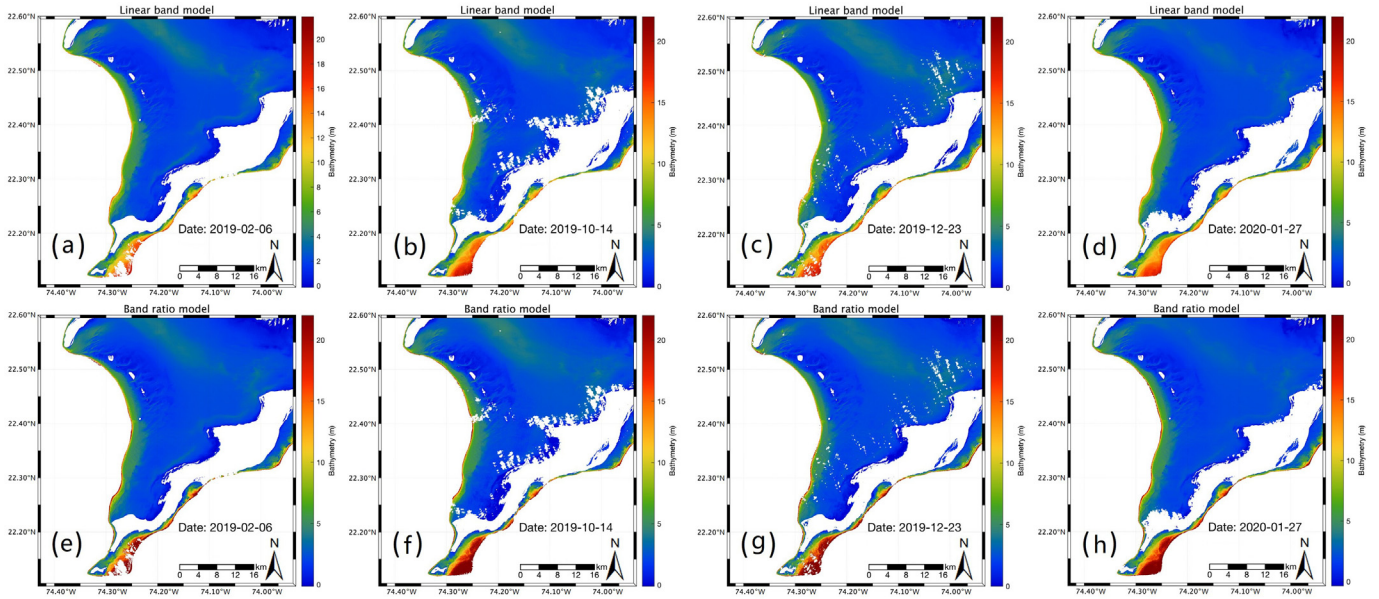


Fig. 13. Shallow water bathymetric maps derived from the two models for the lagoon of Acklins Island and Long Cay using multi-date satellite images. (a) The linear band models on 06/02/2019, (b) on 10/14/2019, (c) on 12/23/2019, and (d) on 27/01/2020, respectively; (e) the band ratio models on 06/02/2019, (f) on 10/14/2019, (g) on 12/23/2019, and (h) on 27/01/2020, respectively. Note that land areas (over the water level), clouds covered areas, and water depths deeper than 22 m were subtracted in maps.

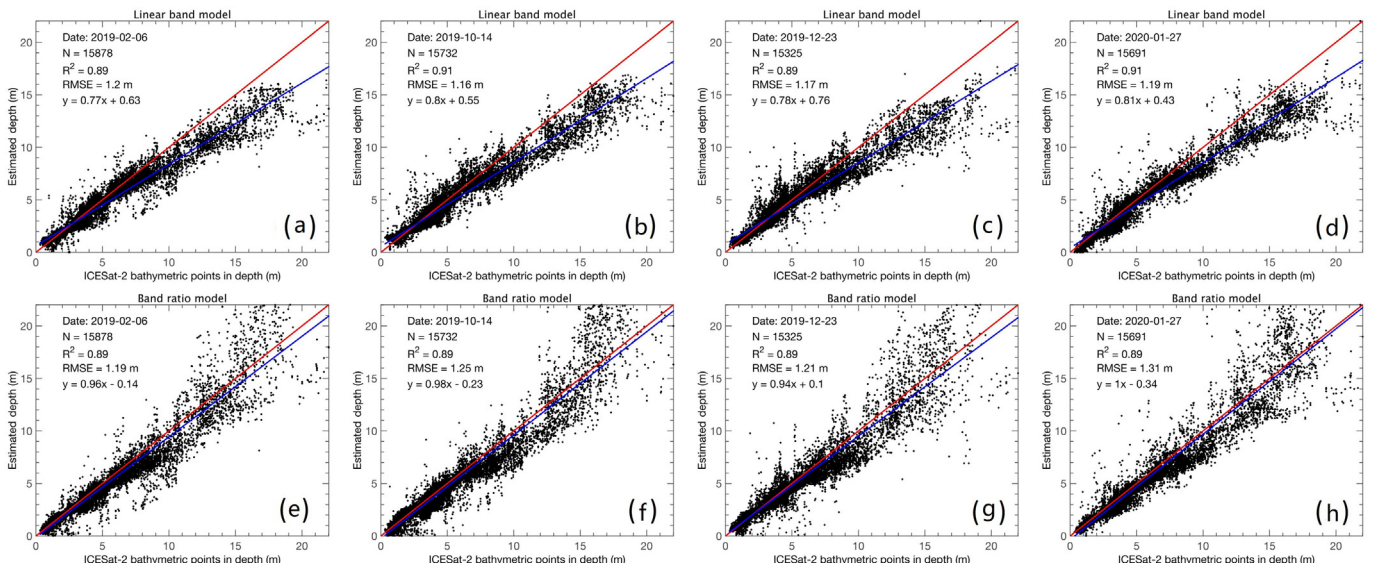


Fig. 14. Error scatter diagrams of retrieved water depths and *in-situ* depths near Acklins Island and Long Cay on four dates. (a) The linear band models on 06/02/2019, (b) on 10/14/2019, (c) on 12/23/2019, and (d) on 27/01/2020, respectively; (e) the band ratio models on 06/02/2019, (f) on 10/14/2019, (g) on 12/23/2019, and (h) on 27/01/2020, respectively. The red line is the 1:1 line, whereas the blue line corresponds to the regression line. N is the number of *in-situ* bathymetric points from the ICESat-2 data, which correspond to green lines in Fig. 2 and were captured in different dates and locations compared with the ICESat-2 training points (red lines in Fig. 2). The regression equations of different models for each date are also involved. (For interpretation of the references to colour in this figure legend, the reader is referred to the web version of this article.)

pre-processed Sentinel-2 images.

In every study area, four-date Sentinel-2 images were used to analyze the spatial-temporal consistency of this proposed approach. Near Yongle Atoll, where the estimated maximum depth is 18 m, the mean R^2 and RMSE of the four-date images in the validation procedure are 0.91 and 1.44 m for the linear model, whereas the mean R^2 and RMSE are 0.85 and 1.85 m for the band ratio model. In the consistency analysis, the mean R^2 and RMSE are 0.97 and 0.77 m for the linear model, whereas the mean R^2 and RMSE are 0.95 and 0.87 m for the band ratio model. Near Acklins Island and Long Cay, where the estimated maximum depth is 22 m, the mean R^2 and RMSE of the four-date images in

the validation procedure are 0.90 and 1.18 m for the linear model, whereas the mean R^2 and RMSE are 0.89 and 1.24 m for the band ratio model. In the consistency analysis, the mean R^2 and RMSE are 0.98 and 0.35 m for the linear model, whereas the mean R^2 and RMSE are 0.97 and 0.48 m for the band ratio model.

The results indicate that, the bathymetric accuracy is generally well, and the RMSE are lower or close to 10% of the maximum depth for the two models with four-date images in two study areas. The consistency of multi-date data is well with mean R^2 of 0.97. The linear band model generally has a slightly better bathymetric accuracy and consistency. A significant difference from the empirical models in previous studies is

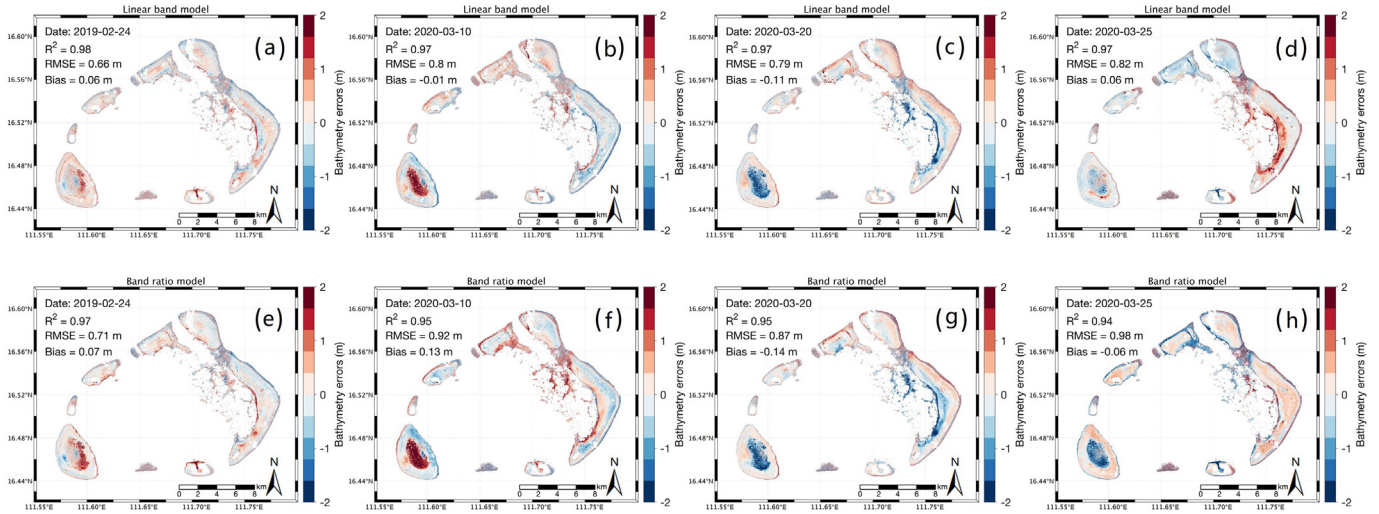


Fig. 15. Spatial difference distributions between the mean of four-date bathymetric maps and single-date bathymetric map near Yongle Atoll. (a) The linear band models on 24/02/2019, (b) on 10/03/2020, (c) on 20/03/2020, and (d) on 25/03/2020, respectively; (e) the band ratio models on 24/02/2019, (f) on 10/03/2020, (g) on 20/03/2020, and (h) on 25/03/2020, respectively.

that this method does not rely on any *in-situ* auxiliary bathymetric points, but uses only satellite-based remotely sensed data. It means that the empirical models using satellite multispectral imagery are no longer limited by the *priori* measurements with the support of the ICESat-2 data. In the future, the ICESat-2 can provide plenty of accurate along-track bathymetric points wherever it flies over, and along with multispectral satellite, we are able to obtain bathymetric maps in shallow water of coastal areas, surroundings of islands and reefs, and inland waters (e.g., rivers, lakes and reservoirs) at a global scale, especially for the remote and sensitive areas without *priori* data.

Declaration of Competing Interest

The authors declare that they have no known competing financial interests or personal relationships that could have appeared to influence the work reported in this paper.

Acknowledgments

This work was supported by the National Science and Technology Major Project [Grant numbers 42-Y20A11-9001-17/18, 11-Y20A12-9001-17/18]; the National Natural Science Foundation of China [Grant number 41801261]; the National Key Research and Development Program of China [Grant numbers 2017YFC1404104, 2017YFC1404100]; the China Postdoctoral Science Foundation [Grant number 2020T130481]; the Key Technology Research and Development Program of Shandong [Grant number 2019GHY112049]; and the Fundamental Research Funds for the Central Universities [Grant number 2042020kf1050]. We sincerely thank the ESA's Sentinel Scientific Data Hub for distributing the Sentinel-2 data, the ESA providing the SNAP software for free, and the Goddard Space Flight Center for distributing the ICESat-2 data. This is publication No. 83 of the Sino-Australian Research Consortium for Coastal Management (previously the Sino-Australian Research Centre for Coastal Management).

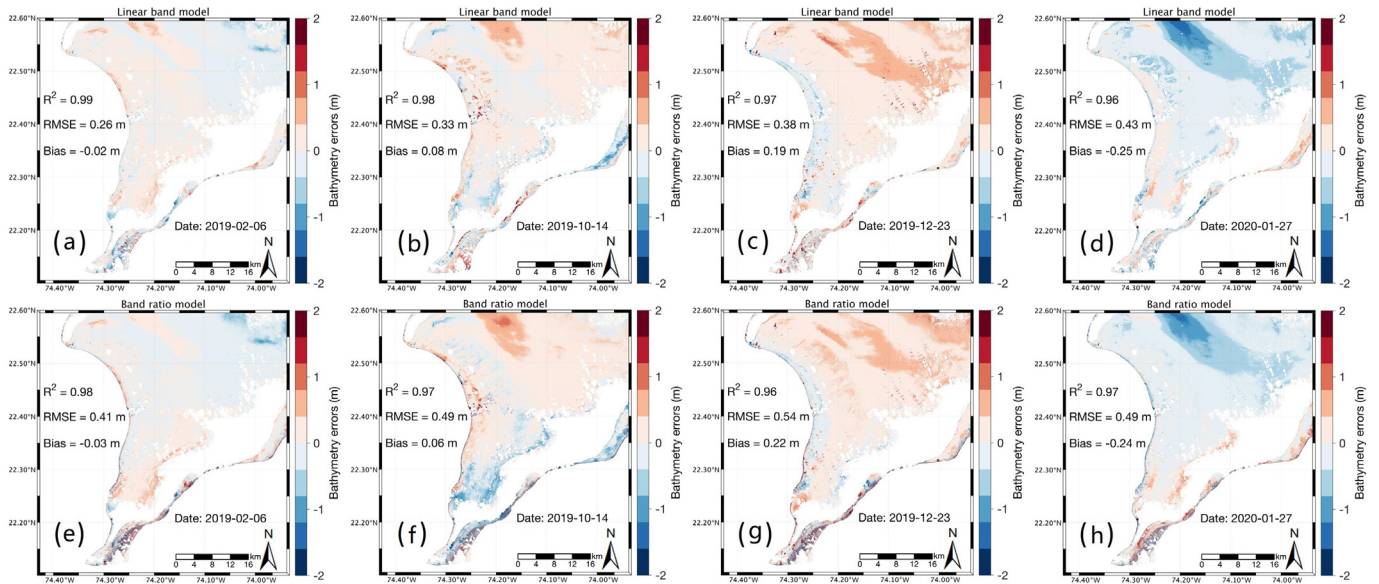


Fig. 16. Spatial difference distributions between the mean of four-date bathymetric maps and single-date bathymetric map near Acklins Island and Long Cay. (a) The linear band models on 06/02/2019, (b) on 10/14/2019, (c) on 12/23/2019, and (d) on 27/01/2020, respectively; (e) the band ratio models on 06/02/2019, (f) on 10/14/2019, (g) on 12/23/2019, and (h) on 27/01/2020, respectively.

Table 2
Comparisons of linear band model and band ratio model in the training, validation, and consistency analysis.

Location	Yongle Atoll (Maximum depth 18 m)						Lagoon near Acklins Island and Long Cay (Maximum depth 22 m)					
	Date	Linear band model R^2	Linear band model RMSE/m	Band ratio model R^2	Band ratio model RMSE/m	Procedure	Date	Linear band model R^2	Linear band model RMSE/m	Band ratio model R^2	Band ratio model RMSE/m	
Training	24/02/ 2019	0.96	1.06	0.95	1.26	Training	06/02/2019	0.93	0.63	0.95	0.42	
	10/03/ 2020	0.95	1.23	0.93	1.41		10/14/2019	0.93	0.60	0.92	0.58	
	20/03/ 2020	0.96	1.07	0.95	1.17		12/23/2019	0.93	0.66	0.92	0.56	
	25/03/ 2020	0.97	0.96	0.93	1.37		27/01/2020	0.93	0.64	0.93	0.52	
	Mean	0.96	1.08	0.94	1.30		Mean	0.93	0.63	0.93	0.52	
	24/02/ 2019	0.93	1.25	0.87	1.75	Validation (by ICESat-2 points with different dates and locations)	06/02/2019	0.89	1.20	0.89	1.19	
Validation (by airborne lidar points near Ganquan Island)	10/03/ 2020	0.91	1.45	0.88	1.67		10/14/2019	0.91	1.16	0.89	1.25	
	20/03/ 2020	0.89	1.61	0.83	1.96		12/23/2019	0.89	1.17	0.89	1.21	
	25/03/ 2020	0.91	1.46	0.81	2.10		27/01/2020	0.91	1.19	0.89	1.31	
	Mean	0.91	1.44	0.85	1.85		Mean	0.90	1.18	0.89	1.24	
	24/02/ 2019	0.98	0.66	0.97	0.71	Consistency analysis	06/02/2019	0.99	0.26	0.98	0.41	
	10/03/ 2020	0.97	0.80	0.95	0.92		10/14/2019	0.98	0.33	0.97	0.49	
Consistency analysis	20/03/ 2020	0.97	0.79	0.95	0.87		12/23/2019	0.97	0.38	0.96	0.54	
	25/03/ 2020	0.97	0.82	0.94	0.98		27/01/2020	0.96	0.43	0.97	0.49	
	Mean	0.97	0.77	0.95	0.87		Mean	0.98	0.35	0.97	0.48	

References

- Adler-Golden, S.M., Acharya, P.K., Berk, A., Matthew, M.W., Gorodetzky, D., 2005. Remote bathymetry of the littoral zone from AVIRIS, LASH, and QuickBird imagery. *IEEE Trans. Geosci. Remote Sens.* 43, 337–347.
- Brando, V.E., Anstee, J.M., Wettle, M., Dekker, A.G., Phinn, S., Roelfsema, C., 2009. A physics based retrieval and quality assessment of bathymetry from suboptimal hyperspectral data. *Remote Sens. Environ.* 113 (4), 755–770.
- Caballero, I., Stumpf, R.P., 2019. Retrieval of nearshore bathymetry from Sentinel-2A and 2B satellites in South Florida coastal waters. *Estuar. Coast. Shelf Sci.* 226, 106277.
- Caballero, I., Stumpf, R.P., Meredith, A., 2019. Preliminary assessment of turbidity and chlorophyll impact on bathymetry derived from Sentinel-2A and Sentinel-3A satellites in South Florida. *Remote Sens.* 11 (6), 645.
- Cahalane, C., Magee, A., Monteys, X., Casal, G., Harris, P., 2019. A comparison of Landsat 8, rapideye and pleiades products for improving empirical predictions of satellite-derived bathymetry. *Remote Sens. Environ.* 233, 111414.
- Casal, G., Monteys, X., Hedley, J., Harris, P., Cahalane, C., McCarthy, T., 2019. Assessment of empirical algorithms for bathymetry extraction using Sentinel-2 data. *Int. J. Remote Sens.* 40 (8), 2855–2879.
- Casal, G., Harris, P., Monteys, X., Hedley, J., Cahalane, C., McCarthy, T., 2020. Understanding satellite-derived bathymetry using Sentinel 2 imagery and spatial prediction models. *GISci. Remote Sens.* 57 (3), 271–286.
- Cerdeira-Estrada, S., Heege, T., Kolb, M., Ohendorf, S., Uribe-Martínez, A., Müller, A., Garza-Pérez, J.R., Ressl, R.A., Aguirre, R., Mariño-Tapia, I., Silva, R., Dubois, R.M., 2012. Benthic habitat and bathymetry mapping of shallow waters in Puerto Morelos reefs using remote sensing with a physics based data processing. In: *IEEE International Geoscience and Remote Sensing Symposium*, pp. 4383–4386.
- Chen, B., Yang, Y., Xu, D., Huang, E., 2019. A dual band algorithm for shallow water depth retrieval from high spatial resolution imagery with no ground truth. *ISPRS J. Photogramm. Remote Sens.* 151, 1–13.
- Cox, C., Munk, W., 1954. Measurement of the roughness of the sea surface from photographs of the sun's glitter. *J. Opt. Soc. Am.* 44 (11), 838–850.
- Dekker, A.G., Phinn, S.R., Anstee, J., Bissett, P., Brando, V.E., Fearn, P., Hedley, J., Klonowski, W., Lee, Z.P., Lynch, M., Lyons, M., Mobley, C., Roelfsema, C., 2011. Intercomparison of shallow water bathymetry, hydro-optics, and benthos mapping techniques in Australian and Caribbean coastal environments. *Limnol. Oceanogr. Methods* 9 (9), 396–425.
- Dong, Y., Liu, Y., Hu, C., Xu, B., 2019. Coral reef geomorphology of the Spratly Islands: a simple method based on time-series of Landsat-8 multi-band inundation maps. *ISPRS J. Photogramm. Remote Sens.* 157, 137–154.
- Dörnhöfer, K., Gege, P., Pflug, B., Oppelt, N., 2016a. Mapping indicators of lake ecology at Lake Starnberg, Germany – first results of Sentinel-2A. In: *Proceedings of “Living Planet Symposium 2016”*, pp. 1–8.
- Dörnhöfer, K., Göritz, A., Gege, P., Pflug, B., Oppelt, N., 2016b. Water constituents and water depth retrieval from Sentinel-2A—a first evaluation in an oligotrophic lake. *Remote Sens.* 8 (11), 941.
- Egbert, G.D., Erofeeva, S.Y., 2002. Efficient inverse modeling of barotropic ocean tides. *J. Atmos. Ocean. Technol.* 19, 183–204.
- Ester, M., Kriegel, H.P., Sander, J., Xu, X., 1996. A density-based algorithm for discovering clusters in large spatial databases with noise. In: *Proceedings of 2nd International Conference on Knowledge Discovery and Data Mining*, pp. 226–231.
- Eugenio, F., Marcello, J., Martin, J., 2015. High-resolution maps of bathymetry and benthic habitats in shallow-water environments using multispectral remote sensing imagery. *IEEE Trans. Geosci. Remote Sens.* 53, 3539–3549.
- Gao, J., 2009. Bathymetric mapping by means of remote sensing: methods, accuracy and limitations. *Prog. Phys. Geogr.* 33 (1), 103–116.
- Garcia, R.A., McKenna, L.I.W., Hedley, J.D., Fearn, P.R.C.S., 2014a. Improving the optimization solution for a semi-analytical shallow water inversion model in the presence of spectrally correlated noise. *Limnol. Oceanogr. Methods* 12, 651–669.
- Garcia, R.A., Fearn, P.R.C.S., McKenna, L.I.W., 2014b. Detecting trend and seasonal changes in bathymetry derived from HICO imagery: a case study of Shark Bay, Western Australia. *Remote Sens. Environ.* 147, 186–205.
- Gholamalifard, M., Kutser, T., Esmaili-Sari, A., Abkar, A.A., Naimi, B., 2013. Remotely sensed empirical modeling of bathymetry in the Southeastern Caspian Sea. *Remote Sens.* 5 (6), 2746–2762.
- Giardino, C., Bresciani, M., Cazzaniga, I., Schenk, K., Rieger, P., Braga, F., Matta, E., Brando, V.E., 2014. Evaluation of multi-resolution satellite sensors for assessing water quality and bottom depth of Lake Garda. *Sensors* 14 (12), 24116–24131.
- Hamilton, S., Hedley, J., Beaman, R., 2015. Derivation of high-resolution bathymetry from multispectral satellite imagery: a comparison of empirical and optimisation methods through geographical error analysis. *Remote Sens.* 7 (12), 16257–16273.
- Hedley, J.D., Harborne, A.R., Mumby, P.J., 2005. Simple and robust removal of sun glint for mapping shallow-water benthos. *Int. J. Remote Sens.* 26 (10), 2107–2112.
- Hedley, J.D., Roelfsema, C., Brando, V., Giardino, C., Kutser, T., Phinn, S., Mumby, P.J., Barrilero, O., Laporte, J., Koetz, B., 2018. Coral reef applications of Sentinel-2: coverage, characteristics, bathymetry and benthic mapping with comparison to Landsat 8. *Remote Sens. Environ.* 216, 598–614.
- Hochberg, E., Andrefouet, S., Tyler, M., 2003. Sea surface correction of high spatial resolution ikonos images to improve bottom mapping in near-shore environments. *IEEE Trans. Geosci. Remote Sens.* 41, 1724–1729.
- Hoegh-Guldberg, O., Mumby, P.J., Hooten, A.J., Steneck, R.S., Greenfield, P., Gomez, E., Harvell, C.D., Sale, P.F., Edwards, A.J., Caldeira, K., Knowlton, N., Eakin, C.M., Iglesias-Prieto, R., Muthiga, N., Bradbury, R.H., Dubi, A., Hatziolos, M.E., 2007. Coral reefs under rapid climate change and ocean acidification. *Science* 318 (5857), 1737–1742.
- Irish, J.L., Lillycrop, W.J., 1999. Scanning laser mapping of the coastal zone: the SHOALS system. *ISPRS J. Photogramm. Remote Sens.* 54, 123–129.
- Jagalingam, P., Hedge, A.V., 2017. Estimation of bathymetry along the coast of Mangalore using Landsat-8 imagery. *Int. J. Ocean. Clim. Syst.* 8 (2), 71–83.
- Jasinski, M.F., Stoll, J.D., Cook, W.B., Ondrusk, M., Stengel, E., Brunt, K., 2016. Inland and near-shore water profiles derived from the high-altitude multiple altimeter beam experimental lidar (MABEL). *J. Coast. Res.* 76, 44–55.
- Katja, D., Anna, G., Peter, G., Bringfried, P., Natascha, O., 2016. Water constituents and water depth retrieval from Sentinel-2a – a first evaluation in an oligotrophic lake. *Remote Sens.* 8 (11), 941.
- Kay, S., Hedley, J.D., Lavender, S., 2009. Sun glint correction of high and low spatial resolution images of aquatic scenes: a review of methods for visible and near-infrared wavelengths. *Remote Sens.* 1 (4), 697–730.
- Kerr, J.M., Purkis, S., 2018. An algorithm for optically deriving water depth from multispectral imagery in coral reef landscapes in the absence of ground-truth data. *Remote Sens. Environ.* 210, 307–324.
- Kulp, S.A., Strauss, B.H., 2019. New elevation data triple estimates of global vulnerability to sea-level rise and coastal flooding. *Nat. Commun.* 10 (1), 1–12.
- Kutser, T., Miller, I., Jupp, D.L.B., 2002. Mapping coral reef benthic habitat with a hyperspectral space borne sensor. *Proceedings of the Ocean Optics XVI* 1–14 Santa Fe.
- Kutser, T., Dekker, A.G., Skirving, W., 2003. Modeling spectral discrimination of great barrier reef benthic communities by remote sensing instruments. *Limnol. Oceanogr.* 48 (Part 2), 497–510.
- Kutser, T., Miller, I.R., Jupp, D.L.B., 2006a. Mapping coral reef benthic substrates using hyperspectral space-borne images and spectral libraries. *Estuar. Coast. Shelf Sci.* 70, 449–460.
- Kutser, T., Vahtmäe, E., Martin, G., 2006b. Assessing suitability of multispectral satellites for mapping benthic macroalgal cover in turbid coastal waters by means of model simulations. *Estuar. Coast. Shelf Sci.* 67, 521–529.
- Kutser, T., Vahtmäe, E., Metsamaa, L., 2006c. Spectral library of macroalgae and benthic substrates in Estonian coastal waters. *Proc. Estonian Acad. Sci. Biol. Ecol.* 55, 329–340.
- Kutser, T., Paavel, B., Kaljurand, K., Ligi, M., Randla, M., 2018. Mapping shallow waters of the Baltic Sea with Sentinel-2 imagery. In: *IEEE/OES Baltic International Symposium (BALTIC)*, pp. 1–6.
- Kutser, T., Hedley, J., Giardino, C., Roelfsema, C., Brando, V.E., 2020. Remote sensing of shallow waters – a 50 year retrospective and future directions. *Remote Sens. Environ.* 240, 111619.
- Kwok, R., Cunningham, G.F., Hoffmann, J., Markus, T., 2016. Testing the ice-water discrimination and freeboard retrieval algorithms for the ICESat-2 mission. *Remote Sens. Environ.* 183, 13–25.
- Lafon, V., Froidefond, J.M., Lahet, F., Castaing, P., 2002. SPOT shallow water bathymetry of a moderately turbid tidal inlet based on field measurements. *Remote Sens. Environ.* 81 (1), 136–148.
- Lee, Z., Carder, K.L., Mobley, C.D., Steward, R.G., Patch, J.S., 1998. Hyperspectral remote sensing for shallow waters. I. A semianalytical model. *Appl. Opt.* 37, 6329–6338.
- Lee, Z., Carder, K.L., Mobley, C.D., Steward, R.G., Patch, J.S., 1999. Hyperspectral remote sensing for shallow waters: 2. Deriving bottom depths and water properties by optimization. *Appl. Opt.* 38, 3831–3843.
- Lee, Z., Casey, B., Arnone, R.A., Weidemann, A.D., Parsons, R., Montes, M.J., Gao, B.-C., Goode, W., Davis, C.O., Dye, J., 2007. Water and bottom properties of a coastal environment derived from Hyperion data measured from the EO-1 spacecraft platform. In: *SPIE*, pp. 16.
- Lesser, M.P., Mobley, C.D., 2007. Bathymetry, water optical properties, and benthic classification of coral reefs using hyperspectral remote sensing imagery. *Coral Reefs* 26, 819–829.
- Li, Y., Gao, H., Jasinski, M.F., Zhang, S., Stoll, J.D., 2019. Deriving high-resolution reservoir bathymetry from ICESat-2 prototype photon-counting lidar and Landsat imagery. *IEEE Trans. Geosci. Remote Sens.* 57 (10), 7883–7893.
- Liu, Y., Deng, R., Li, J., Qin, Y., Xiong, L., Chen, Q., Liu, X., 2018. Multispectral bathymetry via linear unmixing of the benthic reflectance. *IEEE J. Sel. Top. Appl. Earth Obs. Remote Sens.* 11 (11), 4349–4363.
- Lyzenga, D.R., 1978. Passive remote-sensing techniques for mapping water depth and bottom features. *Appl. Opt.* 17 (3), 379–383.
- Lyzenga, D.R., 1981. Remote sensing of bottom reflectance and water attenuation parameters in shallow water using aircraft and Landsat data. *Int. J. Remote Sens.* 2 (1), 71–82.
- Lyzenga, D.R., 1985. Shallow-water bathymetry using combined lidar and passive multispectral scanner data. *Int. J. Remote Sens.* 6 (1), 115–125.
- Lyzenga, D.R., Malinas, N.P., Tanis, F.J., 2006. Multispectral bathymetry using a simple physically based algorithm. *IEEE Trans. Geosci. Remote Sens.* 44 (8), 2251–2259.
- Ma, Y., Liu, R., Li, S., Zhang, W., Yang, F., Su, D., 2018. Detecting the ocean surface from the raw data of the MABEL photon-counting lidar. *Opt. Express* 26 (19), 24752–24762.
- Ma, Y., Xu, N., Sun, J., Wang, X.H., Yang, F., Li, S., 2019. Estimating water levels and volumes of lakes dated back to the 1980s using Landsat imagery and photon-counting lidar datasets. *Remote Sens. Environ.* 232, 111287.
- Manessa, M.D.M., Kanno, A., Sagawa, T., Sekine, M., Nurdin, N., 2018. Simulation-based investigation of the generality of Lyzenga's multispectral bathymetry formula in Case-1 coral reef water. *Estuar. Coast. Shelf Sci.* 200, 81–90.
- Manzo, C., Bresciani, M., Giardino, C., Braga, F., Bassani, C., 2015. Sensitivity analysis of a bio-optical model for Italian lakes focused on Landsat-8, Sentinel-2 and Sentinel-3. *Eur. J. Remote Sens.* 48, 17–32.
- Markus, T., Neumann, T., Martino, A., Abdalati, W., Brunt, K., Csatho, B., Farrell, S., Fricker, H., Gardner, A., Harding, D., Jasinski, M., Kwok, R., Magruder, L., Lubin, D., Lutcke, S., Morison, J., Nelson, R., Neuenschwander, A., Palm, S., Popescu, S.,

- Shumj, C., Schutz, B.E., Smith, B., Yang, Y., Zwally, J., 2017. The ice, cloud, and land elevation satellite-2 (ICESat-2): science requirements, concept, and implementation. *Remote Sens. Environ.* 190, 260–273.
- McGill, M., Markus, T., Scott, V.S., Neumann, T., 2013. The multiple altimeter beam experimental Lidar (MABEL): an airborne simulator for the ICESat-2 mission. *J. Atmos. Ocean. Technol.* 30 (2), 345–352.
- Mishra, M.K., Ganguly, D., Chauhan, P., Ajai, 2014. Estimation of coastal bathymetry using RISAT-1 C-band microwave SAR data. *IEEE Geosci. Remote Sens. Lett.* 11 (3), 671–675.
- Misra, A., Vojinovic, Z., Ramakrishnan, B., Luijendijk, A., Ranasinghe, R., 2018. Shallow water bathymetry mapping using support vector machine (svm) technique and multispectral imagery. *Int. J. Remote Sens.* 39, 4431–4450.
- Mobley, C.D., Sundman, L.K., Davis, C., Bowles, J.H., Downes, T.V., Leathers, R.A., Montes, M.J., Bissett, W.P., Kohler, D.D.R., Reid, R.P., Louchard, E.M., Gleason, A., 2005. Interpretation of hyperspectral remote-sensing imagery by spectrum matching and look-up tables. *Appl. Opt.* 44, 3576–3592.
- Monteys, X., Harris, P., Caloca, S., Cahalane, C., 2015. Spatial prediction of coastal bathymetry based on multispectral satellite imagery and multibeam data. *Remote Sens.* 7 (10), 13782–13806.
- Neuenschwander, A., Pitts, K., 2019. The ATL08 land and vegetation product for the ICESat-2 mission. *Remote Sens. Environ.* 221, 247–259.
- Neuenschwander, A.L., Magruder, L.A., 2019. Canopy and terrain height retrievals with ICESat-2: a first look. *Remote Sens.* 11 (7), 1721.
- Neumann, T., Brenner, A., Hancock, D., Robbins, J., Saba, J., Harbeck, K., Gibbons, A., 2019. Ice, Cloud, and Land Elevation Satellite - 2 (ICESat-2) Project, Algorithm Theoretical Basis Document (ATBD) for Global Geolocated Photons ATL03. Goddard Space Flight Center, Maryland.
- Nicholls, R.J., Cazenave, A., 2010. Sea-level rise and its impact on coastal zones. *Science* 328 (5985), 1517–1520.
- Nie, S., Wang, C., Xi, X., Luo, S., Li, G., Tian, J., Wang, H., 2018. Estimating the vegetation canopy height using micro-pulse photon-counting LiDAR data. *Opt. Express* 26 (10), A520–A540.
- Ohlendorf, S., Müller, A., Heege, T., Cerdeira-Estrada, S., Kobryn, H.T., 2011. Bathymetry mapping and sea floor classification using multispectral satellite data and standardized physics based data processing. In: *Remote Sensing of the Ocean, Sea Ice, Coastal Waters, and Large Water Regions 2011*. 8175. International Society for Optics and Photonics, pp. 817503.
- Paredes, J.M., Spero, R.E., 1983. Water depth mapping from passive remote sensing data under a generalized ratio assumption. *Appl. Opt.* 22, 1134–1135.
- Parrish, C.E., Magruder, L.A., Neuenschwander, A.L., Forfinski-Sarkozy, N., Alonso, M., Jasinsk, M., 2019. Validation of ICESat-2 ATLAS bathymetry and analysis of ATLAS's bathymetric mapping performance. *Remote Sens.* 11, 01634.
- Pereira, P., Baptista, P., Cunha, T., Silva, P.A., Romão, S., Lafon, V., 2019. Estimation of the nearshore bathymetry from high temporal resolution Sentinel-1A C-band SAR data-a case study. *Remote Sens. Environ.* 223, 166–178.
- Petit, T., Bajjouk, T., Mouquet, P., Rochette, S., Vozel, B., Delacourt, C., 2017. Hyperspectral remote sensing of coral reefs by semi-analytical model inversion – comparison of different inversion setups. *Remote Sens. Environ.* 190, 348–365.
- Philpot, W.D., 1989. Bathymetric mapping with passive multispectral imagery. *Appl. Opt.* 28, 1569–1578.
- Pike, S., Tragano, D., Poursanidis, D., Williams, J., Medcalf, K., Reinartz, P., Chrysoulakis, N., 2019. Leveraging commercial high-resolution multispectral satellite and multibeam sonar data to estimate bathymetry: the case study of the Caribbean Sea. *Remote Sens.* 11 (15), 1830.
- Popescu, S.C., Zhou, T., Nelson, R., Neuenschwander, A., Sheridan, R., Narine, L., Walsh, K.M., 2018. Photon counting LiDAR: an adaptive ground and canopy height retrieval algorithm for ICESat-2 data. *Remote Sens. Environ.* 208, 154–170.
- Poursanidis, D., Tragano, D., Reinartz, P., Chrysoulakis, N., 2019. On the use of Sentinel-2 for coastal habitat mapping and satellite-derived bathymetry estimation using downsampled coastal aerosol band. *Int. J. Appl. Earth Obs. Geoinf.* 80, 58–70.
- Raucoules, D., de Michele, M., Idier, D., Smal, F., Foumelis, M., Boulahya, F., Volden, E., Drakopoulou, V., Mujta, P., 2019. Bathysent – a method to retrieve coastal bathymetry from Sentinel-2. In: *IEEE International Geoscience and Remote Sensing Symposium*, pp. 8193–8196.
- Renga, A., Rufino, G., D'Errico, M., Moccia, A., Boccia, V., Graziano, M.D., Aragno, C., Zoffoli, S., 2014. SAR bathymetry in the Tyrrhenian Sea by COSMO-SkyMed data: a novel approach. *IEEE J. Sel. Top. Appl. Earth Obs. Remote Sens.* 7 (7), 2834–2847.
- Shang, X., Zhao, J., Zhang, H., 2019. Obtaining high-resolution seabed topography and surface details by co-registration of side-scan sonar and multibeam echo sounder images. *Remote Sens.* 11 (12), 1496.
- Stumpf, R.P., Holderied, K., Sinclair, M., 2003. Determination of water depth with high-resolution satellite imagery over variable bottom types. *Limnol. Oceanogr.* 48 (1part2), 547–556.
- Su, D., Yang, F., Ma, Y., Zhang, K., Huang, J., Wang, M., 2019. Classification of coral reefs in the South China Sea by combining airborne LiDAR bathymetry bottom waveforms and topographic features. *IEEE Trans. Geosci. Remote Sens.* 57 (2), 815–828.
- Su, D., Yang, F., Ma, Y., Wang, X.H., Yang, A., Qi, C., 2020. Propagated uncertainty models arising from device, environment, and target for a small laser spot airborne LiDAR bathymetry and its verification in the South China Sea. *IEEE Trans. Geosci. Remote Sens.* 58 (5), 3213–3231.
- Su, H., Liu, H., Wang, L., Filippi, A.M., Heyman, W.D., Beck, R.A., 2014. Geographically adaptive inversion model for improving bathymetric retrieval from satellite multispectral imagery. *IEEE Trans. Geosci. Remote Sens.* 52, 465–476.
- Su, H., Liu, H., Wu, Q., 2015. Prediction of water depth from multispectral satellite imagery - the regression kriging alternative. *IEEE Geosci. Remote Sens. Lett.* 12 (12), 2511–2515.
- Tragano, D., Poursanidis, D., Aggarwal, B., Chrysoulakis, N., Reinartz, P., 2018. Estimating satellite-derived bathymetry (SDB) with the google earth engine and Sentinel-2. *Remote Sens.* 10 (6), 859.
- Tsai, B.M., Gardner, C.S., 1982. Remote sensing of sea state using laser altimeters. *Appl. Opt.* 21 (21), 3932–3940.
- Vahtmäe, E., Kutser, T., 2016. Airborne mapping of shallow water bathymetry in the optically complex waters of the Baltic Sea. *J. Appl. Remote. Sens.* 10 (2), 025012.
- Warren, M.A., Simis, S.G.H., Martinez-Vicente, V., Poser, K., Bresciani, M., Alikas, K., Spyarakos, E., Giardino, C., Ansper, A., 2019. Assessment of atmospheric correction algorithms for the Sentinel-2a multispectral imager over coastal and inland waters. *Remote Sens. Environ.* 225, 267–289.
- Westfeld, P., Maas, H.G., Richter, K., Weiß, R., 2017. Analysis and correction of ocean wave pattern induced systematic coordinate errors in airborne LiDAR bathymetry. *ISPRS J. Photogramm. Remote Sens.* 128, 314–325.
- Xu, L.Q., Liu, X.D., Sun, L.G., Yan, H., Liu, Y., Luo, Y.H., Huang, J., 2011. Geochemical evidence for the development of coral island ecosystem in the Xisha archipelago of South China Sea from four ornithogenic sediment profiles. *Chem. Geol.* 286 (3–4), 135–145.
- Yang, F., Bu, X., Ma, Y., Lu, X., Wang, M., Shi, B., 2017a. Geometric calibration of multibeam bathymetric data using an improved sound velocity model and laser tie points for BoMMS. *Ocean Eng.* 145, 230–236.
- Yang, F., Su, D., Ma, Y., Feng, C., Yang, A., Wang, M., 2017b. Refraction correction of airborne LiDAR bathymetry based on sea surface profile and ray tracing. *IEEE Trans. Geosci. Remote Sens.* 55 (11), 6141–6149.
- Yunus, A.P., Dou, J., Song, X., Avtar, R., 2019. Improved bathymetric mapping of coastal and lake environments using Sentinel-2 and Landsat-8 images. *Sensors* 19 (12), 2788.
- Zhang, K., Yang, F., Zhang, H., Su, D., Li, Q., 2017. Morphological characterization of coral reefs by combining lidar and MBES data: a case study from Yuanzhi Island, South China Sea. *J. Geophys. Res. Oceans* 122 (6), 4779–4790.